POLITECNICO DI TORINO

Master's Degree in
PHYSICS OF COMPLEX SYSTEMS

Master's Degree Thesis

Frustration induced chiral supersolidity in ultracold dipolar gases

Supervisor:
Prof. Luca BARBIERO
Cosupervisors:
Prof. Maciej LEWENSTEIN
Joana FRAXANET MORALES

Candidate:

Michele MIOTTO

April 2024

Abstract

Condensed matter physics is a field of physics dealing with systems formed by many elementary constituents that strongly interact among them. It aims at describing the properties of matter, both at the macroscopic and at the microscopic scale, by means of mathematical models that allows to predict the behavior of large groups of atoms. The models developed are often useful in many different frames, as this theory frequently overlaps with atomic physics, chemistry and biophysics. The development of quantum mechanics allowed for the expansion of this discipline into the quantum world, in particular for the study of exotic phases of matter, whose existence is made possible by the counter-intuitive rules of quantum physics. Supersolidity is certainly one of the most interesting and fascinating phases. This state of matter is characterized by a broken translational symmetry, causing a periodic modulation in the local density of particles as in crystals, but it also exhibits a frictionless flow of particles, typical of superfluidity. The theoretical prediction of supersolidity dates back to the 1950s. Nevertheless, its experimental realization came after many decades, that is only in the second half of 2010s. This result has been achieved thanks to the impressive progress in the control of ultracold dipolar gases. At the moment, theoretical predictions and experimental observations are mainly focused to mean field regimes: the possible presence of this state of matter in a deeply quantum regime remains much less understood.

Moreover, chirality is a property present in many different fields of science and it can play a prominent role in several areas of quantum physics, such as hadronic physics and frustrated magnetic systems. It is related to the spontaneous breaking of the time-reversal symmetry in the system under study. We are particularly interested in the observation of chiral phases induced by the presence of geometrical frustration in systems of interacting quantum particles.

In order to accurately consider the role of quantum fluctuations, we use the Density Matrix Renormalization Group algorithm. The latter allows for the extraction of the ground-state properties of one-dimensional systems and will result particularly effective in studying the model that we want to analyze: the 1D frustrated extended Bose-Hubbard model. The latter takes into account hopping processes between nearest and next-nearest neighbor sites, along with both onsite and longer-range interactions. In our analysis we unveil the presence of a novel quantum phase of matter, namely the chiral lattice supersolid. This exotic quantum state features a density-modulated structure together with the properties of superfluids. In addition, time-reversal symmetry is spontaneously broken and finite currents are present between sites, allowing us to identify this supersolid phase as chiral.

Thanks to the progress in the study and control of ultracold dipolar gases, nowadays

it is possible to create such supersolid states in experiments. The setups are based on the use of magnetic atoms, characterized by a strong magnetic moment that allows for the establishment of long-range interactions. These atoms are cooled down to extremely low temperatures and confined in optical lattices by means of counter-propagating laser beams. We provide a proposal for an experimental setup that enables to reproduce the model under study and to realize the phases we detected in our theoretical analysis.

Acknowledgements

I want to express my gratitude to everyone that contributed to the development and the realization of this thesis during the last months.

First of all, I want to thank my supervisor, Prof. Luca Barbiero, for his guide and support throughout all the phases of this work and for offering me to possibility to visit ICFO in the meantime.

A big thank you goes out to the whole Quantum Optics Theory group at ICFO, whose members have been always available to offer help and guidance. In particular, I want to thank the group leader, Prof. Maciej Lewenstein, for accepting me in the group and especially my tutor Joana Fraxanet Morales, whom was extremely pleasant to work with and whose support has been crucial in the creation of this essay.

I also want to acknowledge the computational resources provided by ICFO, which allowed me to perform efficient calculation and produce a large amount of results.

In addition, I care to express my gratitude to both Politecnico di Torino and ICFO for their financial support.

Next to that, big appreciation goes out to all my friends: some of them know me since when I was a kid, some others I met during the last few years, but all of them were fundamental in my life thanks to all the experiences we shared.

Last but probably most important, I want to thank my parents and my family, who have been always very close to me during my whole life and my academic path and they never stopped pushing me to pursue my goals.

Table of Contents

1 Introduction 1

2 Supersolidity 4
- 2.1 Definition and theoretical prediction 4
  - 2.1.1 Supersolidity in ^{4}He 6
- 2.2 Experimental observation 9
  - 2.2.1 Ultracold atoms in optical lattices 9
  - 2.2.2 Cavities and spin-orbit coupling 11
  - 2.2.3 Ultracold dipolar gases 14

3 Bose-Hubbard models and geometrical frustration 23
- 3.1 Bose-Hubbard models 23
  - 3.1.1 1D extended Bose-Hubbard model 27
- 3.2 Geometrical frustration and chirality 30

4 Simulation methods 33
- 4.1 Density Matrix Renormalization Group 34
  - 4.1.1 Infinite DMRG 35
  - 4.1.2 Finite-size DMRG 36
  - 4.1.3 Tensor Networks 39

5 Frustrated extended Bose-Hubbard model 46

6 Results 52
- 6.1 Ground-state phase diagrams 52
  - 6.1.1 Phase diagram at fixed on-site interaction 54
  - 6.1.2 Phase diagram at fixed next-nearest neighbor hopping amplitude 56
- 6.2 Characterization of the chiral phases 57
- 6.3 Order parameters along cuts of phase diagrams 59

6.4 Charge gap 62

7 Outlook and conclusion 66

A Example script for iDMRG with TeNPy 68

Bibliography 71

Chapter 1

Introduction

At the beginning of the 20th century, the basis of physics were shaken by a series of theories and experiments that completely disrupted concepts established in the previous centuries.

The biggest revolution occurred with the development of a theory destined to shape the future of physics in a whole new way: we are referring to quantum mechanics. This game-changing theory was the result of the effort of many scientists that tried to understand the paradoxical aspects of some phenomena at the microscopic level, such as the problem of black-body radiation studied by Max Planck (1901) and the photoelectric effect explained by Albert Einstein (1905), next to the formulation of new atomic models by Ernest Rutherford (1911), Niels Bohr (1913) and Arnold Sommerfeld (1916).

These studies led to an entire new set of concepts, that were used to describe the behaviour of particles and waves at the microscopic scale, which strongly differs from their collective macroscopic properties. The main steps in this direction were made by Louis de Broglie (1924), who highlighted the wave-particle duality, Erwin Schrödinger (1926), whom a renowned equation was named after, Werner Heisenberg with his formulation of the theory in terms of matrices (1925) and the uncertainty principle (1927), and Paul Dirac, who introduced the new powerful bra-ket notation (1930) and first tried to unite quantum mechanics with the theory of relativity.

The first feature of this new theory that stands out is the fact that it contradicts our everyday experience: particles can behave as waves and viceversa; the act of measuring always influences the outcome of an experiment; it is impossible to obtain full information about the state of a microscopic quantum system even with a virtually perfect measurement setup. The most revolutionary consequence is the loss of determinism and this forced the physicists to accept that everything in the microscopic world has to be described in probabilistic terms, which is reflected in the mathematical structure of quantum mechanics. All this gives rise to strange concepts, such as the discreteness of the natural world, and to peculiar phenomena, for instance the tunneling effect, that are inevitably difficult to accept and understand.

A field of physics were some of the most interesting phenomena are made possible by the rules of quantum mechanics is represented by condensed matter physics, in particular in the context of many-body quantum systems. In his groundbreaking article *More is different* (1972) [1] on the theory of broken symmetry, Philip Anderson pointed out that:

> "The behavior of large and complex aggregates of elementary particles, it turns out, is not to be understood in terms of a simple extrapolation of the properties of a few particles. Instead, at each level of complexity entirely new properties appear, and the understanding of the new behaviors requires research which I think is as fundamental in its nature as any other"

The main takeaway of the paper, which has the declared purpose of opposing to the reductionist point of view, is that the individual constituents of an aggregate have a different collective behaviour with respect to how they would behave by themselves. This is a key concept not only in many-body quantum physics, but also in biology, chemistry, social sciences and so on.

Staying within our field of interested, one of the most exciting collective phenomena is superconductivity, first discovered by Kamerlingh Onnes in 1911 and finally explained at microscopic level in 1957 with the famous BCS theory by Bardeen, Cooper and Schrieffer. Below a material-dependent transition temperature, certain metals allow for the coupling of their conduction electrons mediated by phonons, which are the quanta of vibration of the lattice of positive ions. These electrons form the so-called Cooper pairs, which behave as bosons and create a current flow with no electric resistance, so that it never decays in time. This intriguing state of matter is characterized also by non-trivial magnetic properties, which can be exploited for some interesting applications, such as levitating systems.

In the last decades of the past century, it has been realized that the superconducting state is the electronic analogous of another striking phase of matter, discovered decades before: the superfluid state [2]. While in a classical fluid particles move randomly and are indistinguishable one from the other, in superfluids they form a macroscopic wave of matter and move coherently, flowing with no friction and exhibiting an unconventional rotating behaviour [3]. The discovery had been made by J. Allen and A. Misener in 1937 studying liquid ^{4}He [4] and simultaneously by P. Kapitza, who coined the term "superfluid" [5]. The first theory of superfluidity is due to L. Landau, who developed a phenomenological and semi-microscopic theory for ^{4}He at temperatures below 2.17 K [6, 7], for which he won the Nobel

prize in 1962. In the same years, F. London [8] and L. Tizsa [9] realized that this phenomenon has to be related to the accumulation of indistinguishable bosonic particles in the same state such that they all move together coherently, which is nothing but Bose-Einstein condensation (BEC), as later explained by O. Penrose [10].
Across the last years of the 50s and the first years of the 60s, a new idea started to emerge: is it possible to have such a superflow of particles in a system that still keeps an ordered spatial arrangement of its constituents and is thus a solid?
The combination of these two features is what characterizes the supersolid phase of matter and the question above will be the starting point of our work.

In addition to that, we will consider another phenomenon that can enrich the physics of a quantum many-body system: we are talking about geometrical frustration. This concept was defined by G. Toulouse for magnetic systems as a consequence of topological constraints that prevent neighboring spins from adopting a configuration where every bond energy is minimized [11]. In particular, we are interested in how this can induce the spontaneous breaking of time-reversal symmetry, producing states characterized by chiral currents.

The thesis is organized as follows. In Chapter 2, we will introduce the concept of supersolidity and we will revisit the history behind this exciting phase of matter, focusing on the main developments in the field. In Chapter 3, we will describe Bose-Hubbard models, with particular attention to the extended Bose-Hubbard model in the one-dimensional case; after that, we will move to the discussion of geometrical frustration. In Chapter 4 we will present the Density Matrix Renormalization Group algorithm, which represents the most powerful method for simulating strongly correlated systems in one dimension. In Chapter 5, we will consider the frustrated version of the extended Bose-Hubbard model and we will finally introduce our case of study, together with a proposal for the experimental realization of the system. Then, in Chapter 6 we will display the main results obtained, mentioning also the difficulties encountered and the consequent workarounds we implemented. In the end, in Chapter 7 we will wrap things up by summing up the work, highlighting the relevance of our results and proposing possible developments for extending our studies.
Additional information on the code for simulations is delivered in the Appendix A.

Chapter 2

Supersolidity

Supersolidity represents one of the most fascinating phases of matter, as it simultaneously combines the properties of both a solid and a superfluid.

The theoretical understanding of this phenomenon and the experimental observation of such a state has been an important goal within the scientific community. The reason is that it would pave the way towards a deeper understanding of new states of matter characterizing different physical systems. As an example, it has recently been suggested that one of the components of neutron stars could exhibit some rotational properties typical of supersolids [12]. In particular, some anomalies observed in the rotation frequency of pulsars, which are highly magnetized and fast rotating neutron stars, implies that one of the layers of the inner crust is weakly coupled to the rigid rotation of the star. Here, quantized vortices can form as in a superfluid, but still in presence of a density-modulated structure. This example gives an idea of the extent to which the comprehension of this exotic quantum phenomenon can be useful.

However, the supersolid phase is also one of the most elusive quantum states and its actual existence has been questioned until recent years.

In this chapter, we go through the history of this long sought exotic phase from its theoretical prediction to its successful experimental detection. In order to do that, we mainly refer to the reviews by S. Balibar [13], [3] and M. Boninsegni and N. Prokof'ev [14].

2.1 Definition and theoretical prediction

Let us start from the basics, that is by properly defining the notion of supersolidity. In Chapter 1 we mentioned the superfluid state, which is characterized by the presence of a persistent frictionless flow of particles. In three-dimensional systems,

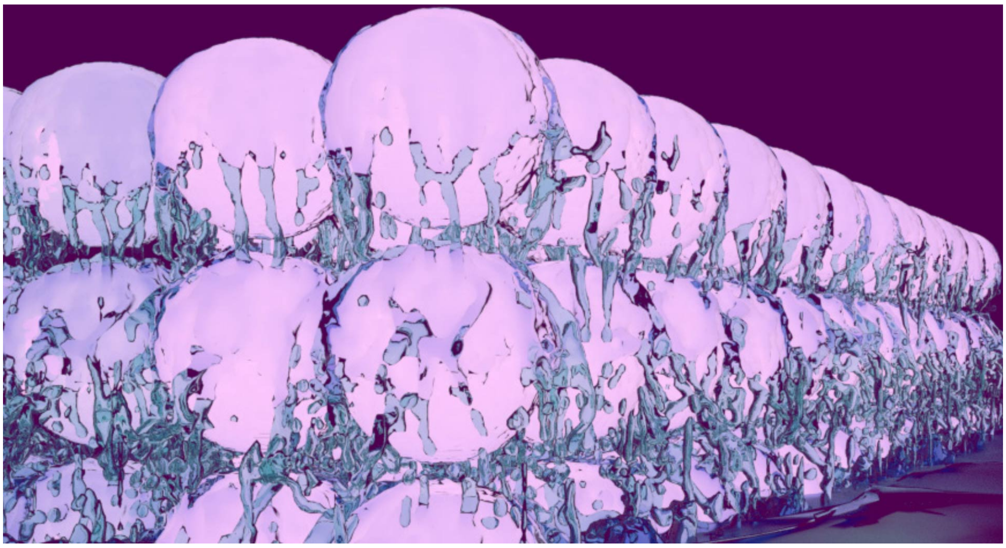

Figure 2.1: Illustration of a supersolid state. Credits to: ETH Zurich / Julian Léonard.

superfludity appears together with Bose-Einstein condensation (BEC), first predicted by Bose [15] and Einstein [16] in 1924. This phenomenon consists in the occupation of only one quantum single-particle state by a finite fraction n_0 of all N particles of the system. This can occur in a macroscopic sample, that is in the thermodynamic limit. The particles that condense are indistinguishable one from the other.

In a many particle system with translation invariance, for instance a fluid, the quantum state where particles condense is the one of a free particle with momentum $\hbar\boldsymbol{k} = 0$. We can now introduce the momentum distribution:

$$\tilde{n}\left(\boldsymbol{k}\right) = \frac{1}{N}\langle\Psi^{\dagger}\left(\boldsymbol{k}\right)\Psi\left(\boldsymbol{k}\right)\rangle \ , \tag{2.1}$$

where $\Psi^{\dagger}\left(\boldsymbol{k}\right)$ and $\Psi\left(\boldsymbol{k}\right)$ are the bosonic creation and annihilation operators, while $\Psi^{\dagger}\left(\boldsymbol{k}\right)\Psi\left(\boldsymbol{k}\right)$ is the number operator for particles of momentum $\hbar\boldsymbol{k}$. Thus, when Bose-Einstein condensation occurs, we have $\tilde{n}\left(\boldsymbol{k}=0\right) = n_0$. By applying a Fourier transform to the momentum distribution, we obtain the following order parameter in real space:

$$n\left(\boldsymbol{r},\boldsymbol{r'}\right) = n\left(\boldsymbol{r}-\boldsymbol{r'}\right) = \langle\Psi^{\dagger}\left(\boldsymbol{r}\right)\Psi\left(\boldsymbol{r'}\right)\rangle \ . \tag{2.2}$$

It can be shown that $n\left(\boldsymbol{r}-\boldsymbol{r'}\right) \to n_0$ for $|\boldsymbol{r}-\boldsymbol{r'}| \to \infty$. This means that, in the thermodynamic limit, a state of a system where a particle is added at position $\boldsymbol{r}$ has a quantum superposition with another state where an identical particle is removed at position $\boldsymbol{r'}$, with $|\boldsymbol{r}-\boldsymbol{r'}|$ arbitrarily large. Therefore, particles form a macroscopic wave of matter and they are delocalized in space. The finiteness of (2.2) signals the spontaneous breaking of a continuous U(1) symmetry, present in the phase factor of single-particle quantum states. This corresponds to the establishment of the so-called off-diagonal long-range order (ODLRO), which is the trademark of superfluidity.

Thanks to this feature, a superfluid flows without friction and exhibits unconventional rotating properties. In particular, if we put a superfluid in a slowly rotating bucket, it stays completely at rest: there is no friction with the moving wall that can set the system in motion. Instead, if a certain critical rotation speed is reached, some rotation occurs within the superfluid in the form of quantized vortices.

Since later we will work with a one-dimensional system, it is important to highlight that the well-known Mermin-Wagner theorem prevents the spontaneous breaking of continuous symmetries at finite temperature in dimensions $d \leq 2$ [17, 18]. Indeed, in a 1D chain the order parameter (2.2) cannot be finite for $|\boldsymbol{r} - \boldsymbol{r'}| \to \infty$ and no superfluidity exists in the thermodynamic limit. However, a superfluid phase can still be defined for finite-size systems and it is associated to a power-law decay with distance of (2.2), much slower than the exponential decay typical of insulating phases. This is the concept of superfluidity that we will use when dealing with 1D models.

Let us now consider a solid with a crystalline structure. Here, the particles forming the solid are arranged in a periodic structure. This state clearly breaks the translational invariance and thus the system is rigid and resistant to shear. In this case, it is said that the system exhibits diagonal long-range order (DLRO). Note that, for a correct definition of a solid, the breaking of translational symmetry has to occur spontaneously due to the interactions among its elementary constituents.

Moving to the case of a quantum solid, it is known that particles fluctuate around their equilibrium position and some atoms may exchange places with neighboring ones, with the possibility of creating a partial flow of atoms through the otherwise rigid network. If this flow becomes superfluid, a fraction of particles moves without friction and, in the case of rotation, some of the mass stays at rest as the remaining part rotates. Therefore, a part of the system is delocalized and the remainder is localized, corresponding to the coexistence of both DLRO and ODLRO: we thus have a supersolid.

An illustration of this puzzling phase of matter is shown in Fig. 2.1.

2.1.1 Supersolidity in ^{4}He

O. Penrose and L. Onsager have been the first to predict the existence of supersolids in their seminal paper in 1956 [19]. However, they concluded that no ODLRO can

exist in a crystalline solid because crystallization or other causes determine particles localization, which prevents the establishing of quantum coherence, peculiar of superfluid matter. Nevertheless, they did not find any formal proof that completely rules out the presence of OLDRO in ordered structures. Indeed, in the following years, E. Gross showed how a superfluid described by a nonlinear classical field equation may feature, at least in principle, a density wave modulation [20, 21]. This can be seen as the first theory of supersolidity, but Gross's results were mostly overlooked due to an incomplete understanding of the conditions needed for their validity.
A few years later, in 1962, C. Yang proposed the existence of the supersolid phase in ^{4}He crystals [22] and his argument was then revisited by A. Leggett, who also suggested an experimental setup for the measurement of the superfluid flow in solid helium, exploiting the anomalous rotation that such a system should display [23].

Another well-known scenario was proposed by A. Andreev and I. Lifshitz [24] and G. Chester [25]. In their picture, an high mobility is associated to vacancies or interstitials, which are called "zero-point defects" since they can be present even in the ground-state of a quantum system due to quantum fluctuations. These defects can hop from site to site and form a BEC of vacancies and give rise to a superfluid flow: in fact, a flow of vacancies in a certain direction corresponds to a flow of particles in the opposite one. This scenario has later been proved to be the only one possible in perfect continuous crystals [26].

Despite the formulation of these scenarios for the emergence of supersolidity, a clear experimental observation was not achieved for many decades and the interest around this fascinating phenomenon faded more and more.
However, things changed in 2004, when E. Kim and M. Chan claimed the observation of supersolid properties in solid ^{4}He at temperatures below 250 mK [27, 28]. They used a torsional oscillator containing a cylindrical cell with an annular space filled with a material, suspended from a torsion rod, see Fig. 2.2. At resonance, the period of the oscillator is directly related to the rotational inertia of the material through a known relation. If the annular space is filled with liquid helium, then the superfluid transition is marked by a shift in the resonance period of the oscillator, due to the decrease in the inertia: if the oscillation velocity does not exceed the critical value, the superfluid stays at rest even if the walls oscillate. In their experiment, Kim and Chan considered temperatures below the transition point from liquid to solid for ^{4}He and they observed a shift in the oscillator period, whose magnitude indicated that only a very small fraction of the total mass was superfluid. This was in agreement with the prediction by Leggett that we mentioned above.

This discovery by Kim and Chan created a renovated enthusiasm in the search for

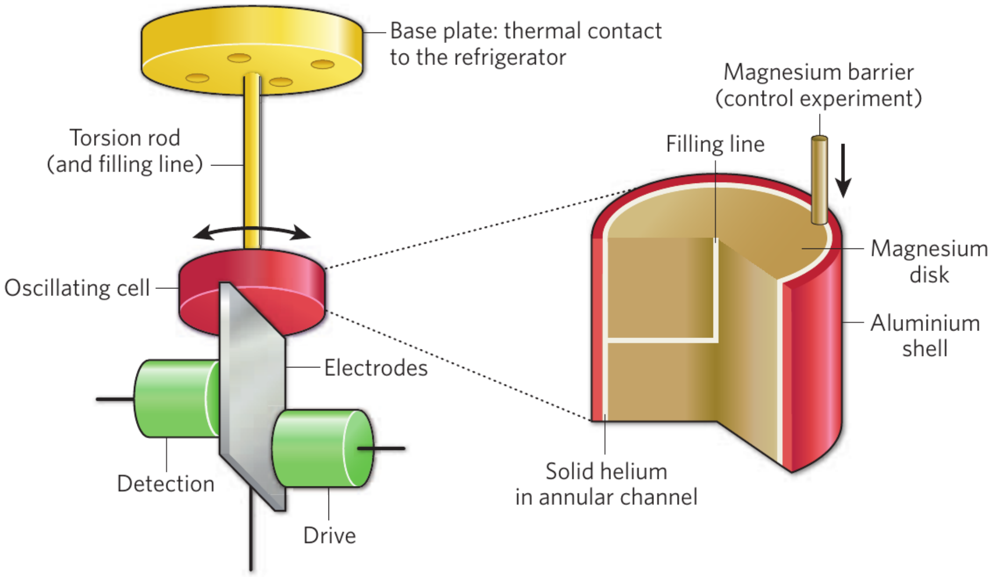

Figure 2.2: Schematics of the experimental setup in the torsional oscillator experiment by Kim and Chan. Taken from [3].

supersolids, but the validity of their findings was questioned. First of all, concerning the nature of supersolidity, some Monte-Carlo simulations seemingly proved that the Andreev-Lifschitz-Chester scenario of spontaneous creation of vacancies was not possible in solid helium, though these results were not universally accepted [29]. Instead, a fundamental role could be played by other defects, such as dislocation cores and grain boundaries, where local stresses naturally give form to vacancies. This was seemingly confirmed by experiments studying both a.c. [30, 31] and d.c. [32, 33] mass flows, therefore associating the supersolid behavior observed by Kim and Chan to the presence of disorder in the sample.
In addition to that, it was also observed that the properties of solid ^{4}He were influenced by the presence of ^{3}He impurities, which causes an unexpected stiffening of the solid as the mass flow increases [34, 35]. Indeed, the mobility of dislocations should depend on temperature and ^{3}He concentration, because these impurities should pin dislocations locally below a certain temperature, thus making the solid more rigid.

Following the doubts cast on the validity of their 2004 experiment, Chan's group carried it out again in 2012 with an improved setup that was completely free from any bulk solid shear modulus stiffening effect [36]. This time, they did not observe any shift in the resonance period of the oscillator, in opposition to their previous controversial results.

This was a strong blow to the excitement around supersolidity, as the material where it was predicted decades before, namely solid ^{4}He, was finally ruled out as a possible host of this fascinating phenomenon.

2.2 Experimental observation

After the unsuccessful search for supersolids in solid ^{4}He, the concept of supersolidity has been generalized in order to include also other types of superfluids that break the translational symmetry. In particular, the progress in the experimental control of ultracold atomic systems in optical lattices opened a new path for the study of exotic phases of matter in regimes that were not accessible before.
After reviewing the basics of this technique, we go through the most relevant experiments with ultracold atoms that brought to the realization of supersolidity.

2.2.1 Ultracold atoms in optical lattices

Laser beams offer a very useful tool for the manipulation of atoms, which can be cooled down to the desired temperature or trapped by counter-propagating beams in different geometries. We are particularly interested in the creation of periodic optical lattices, which provide an excellent platform for the simulation of quantum many-body systems. For this purpose, we mainly refer to the reviews by D. Jaksch and P. Zoller [37], C. Gross and I. Bloch [38].

The starting point for the realization of an optical lattice potential is to superimpose two counter-propagating laser beams with $E_{\pm}\left(\boldsymbol{x},t\right)=E_0 e^{\pm ikx}$ along the x-direction. Here, E_0 is the field amplitude, $k=2\pi/\lambda$ is the wave number with λ the wavelength. The same can be done in directions y and z, obtaining a three-dimensional potential with:

$$V\left(\boldsymbol{x}\right)=V_{0x}\cos^2\left(kx\right)+V_{0y}\cos^2\left(ky\right)+V_{0z}\cos^2\left(kz\right)\ , \tag{2.3}$$

where V_{0j} is the depth of the potential in direction j, which can be tuned by setting the intensity of the corresponding pairs of laser beams. The laser setup can be easily controlled to obtain many different lattice geometries.
The lattice can be loaded with ultracold gases and an additional slowly varying potential $V_T\left(\boldsymbol{x}\right)$, for instance created by a magnetic trap, is then used to confine the particles in a certain region of space. It is desirable to have a small lattice spacing so that particles can move through the lattice by tunneling from one site to another. An external magnetic field can be exploited to tune the interactions between atoms via Feshbach resonances [39], which enable one to change their scattering length.

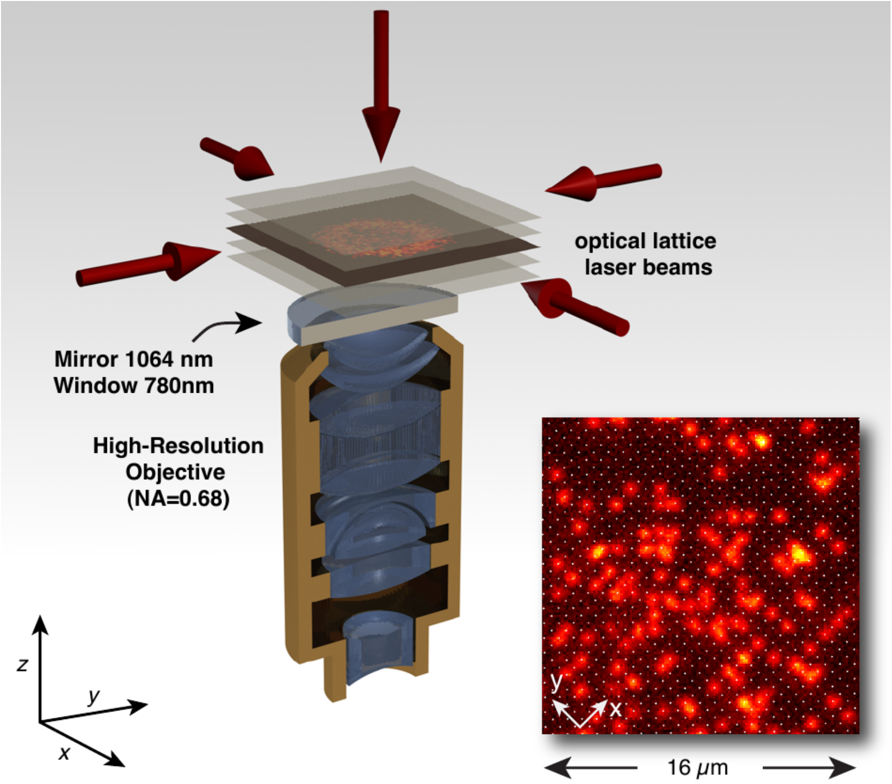

Figure 2.3: Vertical section of a quantum gas microscope scanning 2D layers of an optical lattice. Lower right: fluorescence image obtained. The white dots indicate the underlying lattice and allow to faithfully reconstruct the single-site occupation, even in dense areas. Taken from [40].

In this frame, a fundamental role is played by quantum gas microscopes. First developed for bosonic Rubidium atoms [40, 41], this technology allows for single-site resolved observation of individual atoms via a high resolution microscope objective. The detection is based on the collection of fluorescence photons scattered during in-trap laser cooling of particles. An illustration of a quantum gas microscope with a single-site resolved image is shown in Fig. 2.3.
After its realization, this type of microscope was soon enriched with tools for precise manipulation of atoms, enabling local control of individual particles.

The first strongly correlated lattice model to have been realized by using ultracold atoms in optical lattices is the much celebrated Bose-Hubbard model [42], which will be discussed in Chapter 3.
Nowadays, these platforms allow to simulate many different models, both in the case of bosonic and fermionic atoms. In particular, we highlight the possibility to

include long-range interactions in these setups by using ultracold dipolar gases, formed by magnetic atoms: as we will explain in the following, this was key in the experimental realization of supersolidity.

2.2.2 Cavities and spin-orbit coupling

A line of research is aimed at finding supersolids in systems where continuous symmetries are broken, since this leads to an infinite number of degenerate ground-states that can evolve from one to another without energy cost: these systems are highly susceptible to fluctuations [43].

In an experiment carried out in 2016, the members of Quantum Optics group at ETH Zurich considered a BEC of ^{87}Rb atoms dispersively coupled to the modes of two optical cavities [43] and illuminated by a 1D transverse pump lattice. With this setup, schematically shown in Fig. 2.4(a), they were able to introduce a continuous symmetry in the system as the product of the two discrete spatial ones created by the cavities. In fact, by increasing the coupling to each cavity, a phase transition to self-organized states occurs: the latter are characterized by atomic ordering accompanied by intracavity light fields with parity symmetry. A suitable combination of these two $\mathbb{Z}_2$ symmetries is used to achieve one U(1) continuous symmetry, as the latter is the symmetry present in a superfluid.

The system is microscopically modeled by considering Raman processes between transverse pump and cavity modes that coherently transfer atoms between the motional ground-state and excited momentum states. This causes a split of their energy levels into $\hbar\omega_+$ and $\hbar\omega_-$, determined by the angle between the cavities. The picture can be described by the following Hamiltonian:

$$\begin{aligned} H/\hbar = \sum_{i=1}^{2} \Big[& -\Delta_i a_i^\dagger a_i + \omega_+ c_{i+}^\dagger c_{i+} + \omega_- c_{i-}^\dagger c_{i-} \\ & + \frac{\lambda}{\sqrt{N}} \left(a_i^\dagger + a_i \right) \left(c_{i+}^\dagger c_0 + c_{i-}^\dagger c_0 + h.c. \right) \Big] \end{aligned} \tag{2.4}$$

with N the atom number and $i \in \{1,2\}$ indicating the two cavities. Atoms are described by atomic creation and annihilation operators: $c_0^\dagger$ and c_0 for the motional ground-state, $c_{i+}^\dagger$ and c_{i+} for the high-energy states, $c_{i-}^\dagger$ and c_{i-} for the low-energy ones. Photon fields are described in terms of photonic annihilation and creation operators $a_i^\dagger$ and a_i, while $\Delta_i = \omega_P - \omega_i$ represents the detuning between the resonance frequency ω_i of cavity i and the transverse pump laser frequency ω_P.

By measuring the mean intracavity photon number $\bar{n_i} = |\alpha_i|^2$ as a function of the detunings, the authors observed the emergence of a self-organized phase for each cavity, the both of them exhibiting phase coherence and thus constituting a

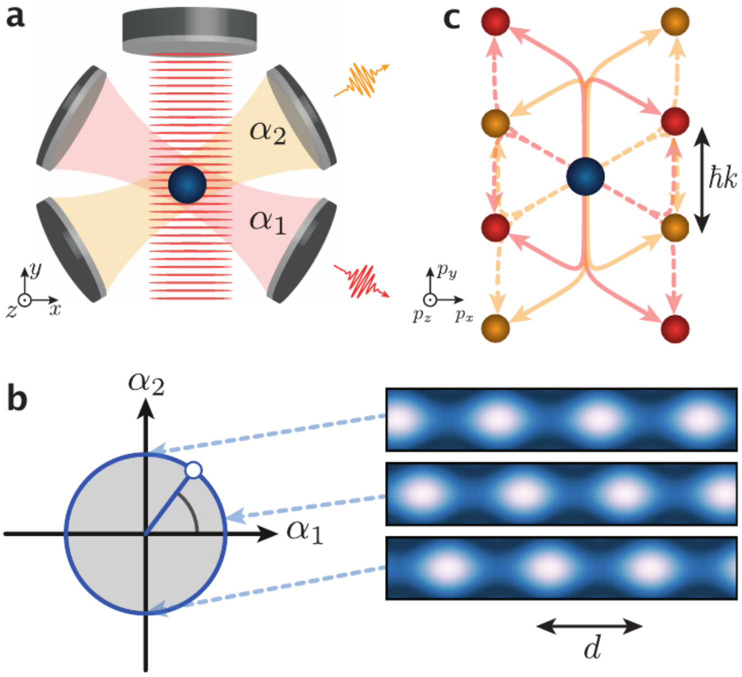

Figure 2.4: Panel **a**: BEC (blue) trapped at the intersection of two optical cavities crossing at an angle of 60° and exposed to a 1D optical lattice induced by a transverse pump beam. The modes of the cavities are shaded in red and yellow, while α_1 and α_2 are the coherent field amplitudes of the respective scattered photons. Panel **b**: on the left, the two individual parity symmetries are combined to a U(1) symmetry, resulting in a circular ground-state manifold in terms of the parameters α_1 and α_2. On the right, the interference potential of the cavity fields with the transverse pump field is d-periodic and moves continuously along the x-axis when changing the angle in the (α_1, α_2) plane. Here, $d = \lambda_P / \sin(60°)$ where λ_P is the wavelength of the transverse pump beam. Panel **c**: atomic momentum states associated with coherent scattering processes between the transverse pump and the two cavities, starting from the ground-state at zero momentum. Solid and dashed lines correspond to creation and annihilation respectively of a cavity photon with momentum $\hbar k$. Taken from [43].

lattice supersolid, as shown in Fig. 2.5. In addition to that, also the existence of an intermediate doubly self-organized phase related to both cavities was witnessed, so that there is no direct transition between the two aforementioned phases, as can be seen in Fig. 2.6.

At the same time, Wolfgang Ketterle's group at Massachusetts Institute of

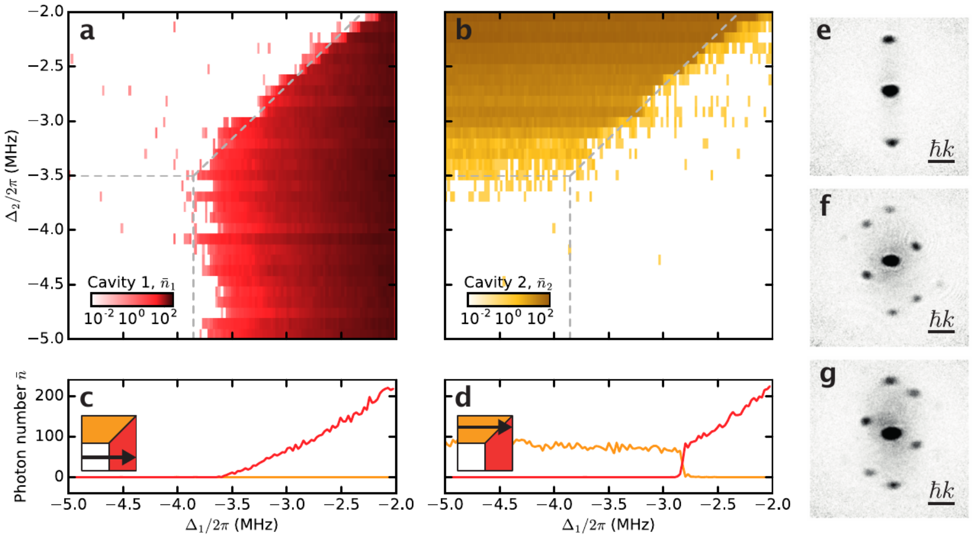

Figure 2.5: Panels **a**, **b**: mean intracavity photon numbers as a function of cavity-pump detunings for constant transverse pump lattice. Panels **c**, **d**: mean intracavity photon numbers as a function of Δ_1 for two fixed values of Δ_2, as signaled in the insets. Panels **e**, **f**, **g**: scale of gray absorption images of atomic momentum distribution in the normal phase (**e**) and the two self-organized phases (**f**, **g**). Taken from [43].

Technology studied a BEC of ^{23}Na atoms with spin-orbit coupling [44]. The action of this coupling is shown to be equivalent to a spin-flip process with momentum transfer, see Fig. 2.7(a), and can be implemented for ultracold atoms by using two-photon Raman transitions between the two spin states. Indeed, the system is described by the following single-particle Hamiltonian:

$$H = \frac{\mathbf{p}^2}{2m} + \begin{bmatrix} 0 & \beta e^{2i\alpha x} \\ \beta e^{-2i\alpha x} & 0 \end{bmatrix} , \tag{2.5}$$

where the second term represents a spin-flip process with a momentum transfer of 2α, with β being the strength of the coupling.

If we have a BEC with equal populations in the two spin states, there is no spatial interference because the states are orthogonal. The introduction of spin-orbit coupling gives two momentum components to each spin component, forming a stationary spatial interference pattern, as shown in Fig. 2.7(a), and this can be observed via Bragg scattering [45], see Fig.2.7(b). Clearly, this phase spontaneously breaks the continuous translational symmetry of the two condensates and it is identified as a stripe supersolid phase.

If a longitudinal Zeeman term $\delta_0\sigma_z$ is added to (2.5), a rich phase diagram can

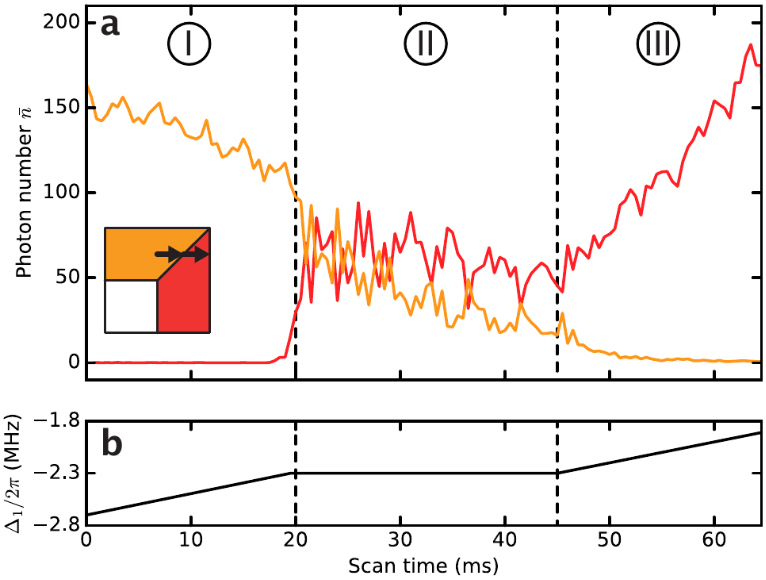

Figure 2.6: Panel **a**: mean intracavity photon numbers for the frequency ramp in panel **b** along the cut indicated in the inset. Red line refers to cavity 1, yellow line to cavity 2. Taken from [43].

be studied as a function of δ_0 and β: a mean-field version of this is shown in Fig. 2.8. The stripe supersolid phase is present for low values of the detuning $|\delta_0|$, while for increasing values a transition to a magnetized phase, with up or down spins, occurs. As the strenght β increases, the stripe phase region becomes thinner until only magnetized phases are possible. For even higher coupling strength, the magnetization vanishes and a single minimum phase should be observed.

However, it is evident that in both these cases, the density modulation is externally imposed through the underlying optical potentials and it does not arise spontaneously due to interactions in the system. Therefore, the translational symmetry is broken ”by hand” and not spontaneously: one of the main consequences is that the modulation present in these phases is infinitely stiff. For this reason, the actual supersolid character of these phases has been object of debate since the publication of the respective articles.

2.2.3 Ultracold dipolar gases

The advancements in the understanding and controlling of systems of ultracold dipolar atoms offered a new promising platform for the experimental realization of supersolids. Indeed, in dipolar gases the emergence of this exotic phase of

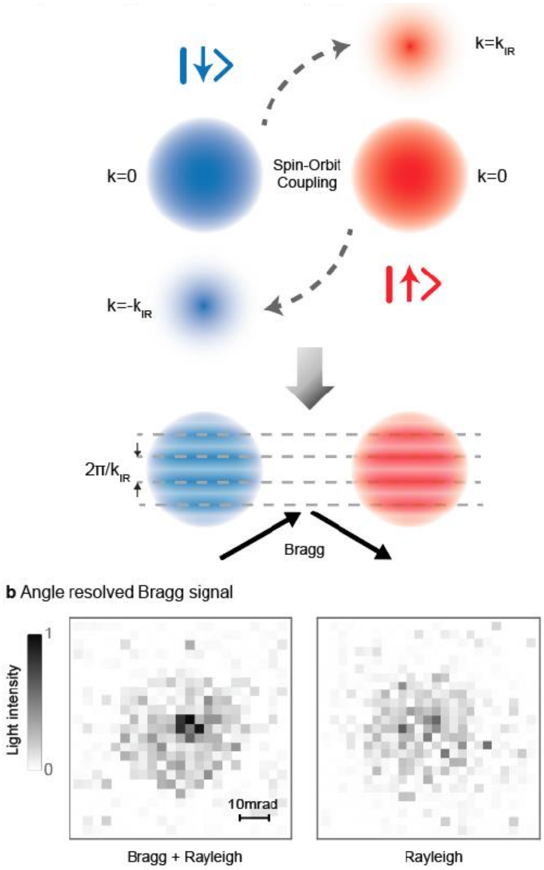

Figure 2.7: Panel **a**: starting from condensates in the two states at zero momentum, spin-orbit coupling adds momentum components $\pm\hbar k_{IR}$ of the opposite spin state to their spin components. A spatial density modulation of period $2\pi/k_{IR}$ arises due to matter-wave interference. Here, $\hbar k_{IR}$ is the recoil momentum from a single infrared photon. Panel **b**: average over seven shots of detection of the stripe phase with angle-resolved light scattering. On the left, a BEC with spin-orbit coupling exhibits both Bragg and Rayleigh scattering due to the density modulation. On the right, a BEC with spin-orbit coupling only shows Rayleigh scattering, since no periodic modulation is present. Taken from [44].

matter is just the result of interparticle interactions: thus, phonon modes of the periodic modulation are allowed like in classical solids and this implies that the aforementioned issue regarding stiffness is not present in such systems [46].

Before discussing the main experiments on this platform and the corresponding results, let us briefly review the progress with dipolar gases up to now, referring to a recent review by Recati and Stringari [47].

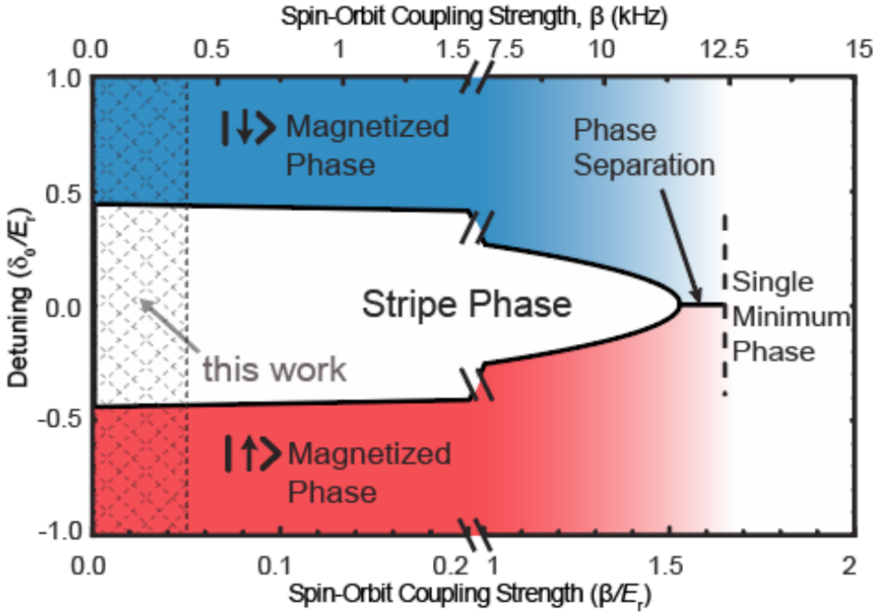

Figure 2.8: Mean-field phase diagram of a spin-orbit coupled BEC as function of detuning δ_0 and spin-orbit coupling strength β. The area shaded in gray represents the region of the parameter space explored in the experiment. E_r is the ^{23}Na recoil energy in the setup. Taken from [44].

Due to the long-range and anisotropic nature of the dipolar force, ultracold dipolar gases behave quite differently with respect to usual superfluids with short-range interactions. In fact, the presence of strong long-range interactions allows for the breaking of translational symmetry, while still conserving quantum coherence, as required for supersolidity [48, 49].

Thanks to the presence of Feshbach resonances [39] in magnetic dipolar atoms, the scattering length can be tuned in order to obtain a suitable value of the ratio between the dipole-dipole and the short-range interaction strengths, thus enabling also the realization of supersolids.

A crucial role in the theory of supersolids in dipolar gases is played by first-order beyond-mean-field corrections, known as Lee-Huang-Yang (LHY) corrections [51]. Indeed, they stabilize the system beyond the collapse due to instability predicted by mean-field theories [52]. This allows for the formation of self-bound droplets in dipolar gases [50, 53, 54], see Fig. 2.9, and also in binary mixtures of BEC gases with attractive interactions [55, 56], which however do not present any feature of supersolidity.

In 2019, three different experimental groups in Stuttgart, Pisa and Innsbruck

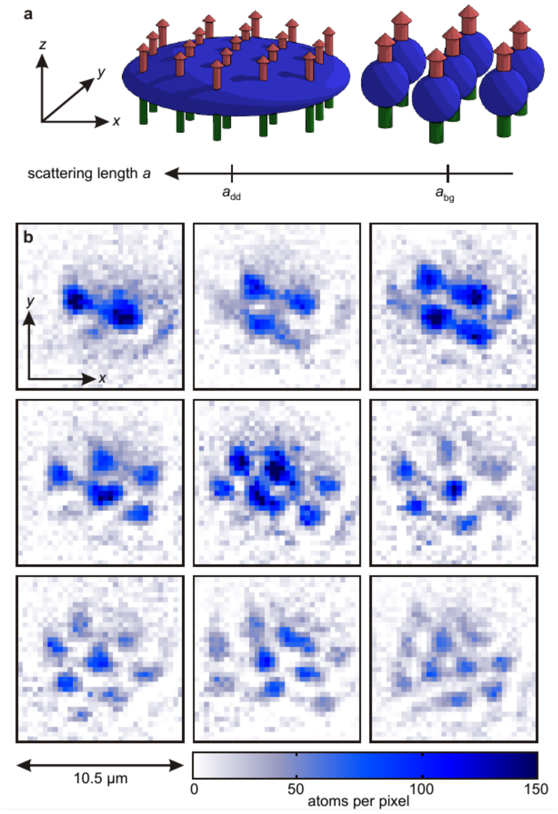

Figure 2.9: Panel **a**: schematics of the experimental procedure from a stable strongly dipolar BEC in a pancake-shaped trap to clustered droplets in a triangular pattern by decreasing the scattering length. Panel **b**: single-shot in-situ images of droplets, from 2 to 10 droplets. The color code indicates the number of atoms per pixel of the image. Taken from [50].

successfully observed a supersolid phase in a cigar-shaped geometry in the form of a coherent array of such quantum droplets, for a small range of values of the scattering length that had been identified through numerical simulations [57]. Let us briefly go through the respective setups and findings.

In Stuttgart, they theoretically studied the supersolid properties of a trapped dipolar gas of ^{162}Dy atoms in a 1D geometry, within the framework of the extended Gross-Pitaevskii equation (eGPE) [58]. The choice of Dysprosium is due to the fact that it is the magnetic atom with the strongest magnetic moment, which implies the presence of a very strong dipolar interaction. Their simulations revealed the existence of 3 different regimes for the ground-state, depending on the scattering length a_s of atoms in the gas. In particular, a Bose-Einstein condensate for large

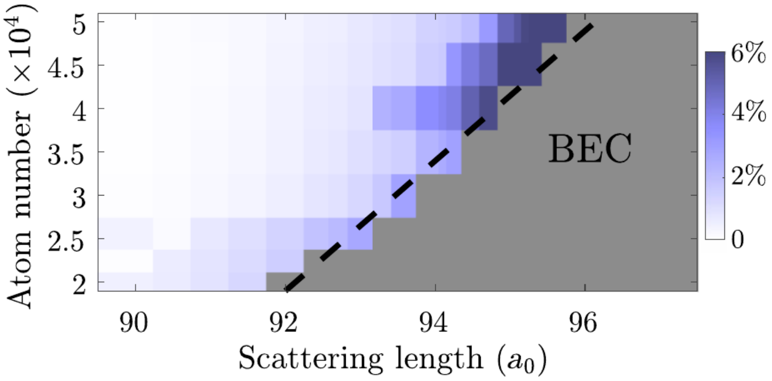

Figure 2.10: Ground-state phase diagram of ratio in (b) as a function of scattering length and atom number. The color code indicates the value of the ratio between first minimum and center peak height of local density of the ground-state. Taken from [58].

values of a_s, and two density-modulated phases: an array of isolated quantum droplets for low values and, most interestingly, a chain of coherent droplets for a narrow intermediate range of a_s. In Fig. 2.10, we report the phase diagram as a function of the scattering length and the atom number. One can clearly identify a phase boundary where density-modulated phases are energetically convenient, first as coherent droplets then as isolated ones. In addition to that, for higher atom numbers, the number of droplets increases and so does their overlap, enhancing the supersolid character of the intermediate phase. For the experimental investigation of this coherent phase, they considered a dipolar BEC with approximately 4.5×10^4 ^{162}Dy atoms at a temperature below 20 nK in a tubular trap and they varied the

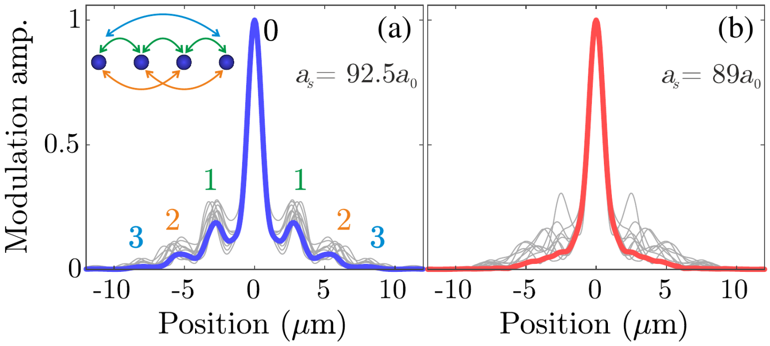

Figure 2.11: Fourier transform of integrated interference pattern after 30 ms time-of-flight for $a_s = 92.5a_0$ (a) and $a_s = 89a_0$ (b) for the ground-state with 4.5×10^4 atoms. Taken from [58].

scattering length by means of a magnetic field gradient. The experiment confirmed the existence of this transient supersolid phase, both with in-situ density modulation and interference pattern of multiple matter waves after time-of-flight analysis. In Fig. 2.11, we report an example of the Fourier transform of the integrated interference pattern after time-of-flight, interpreted as the momentum distribution of atoms, for different values of a_s. On the left panel, we see that side peaks appear always at the same position with similar amplitudes in every realization, each one drawn in gray, while on the right panel their position and amplitude change randomly. Therefore, we can say that the left picture represents a coherent droplet phase, as the side peaks corresponds to successive neighbors coherence, even up to next-next-next nearest neighbors for the chosen atom number.

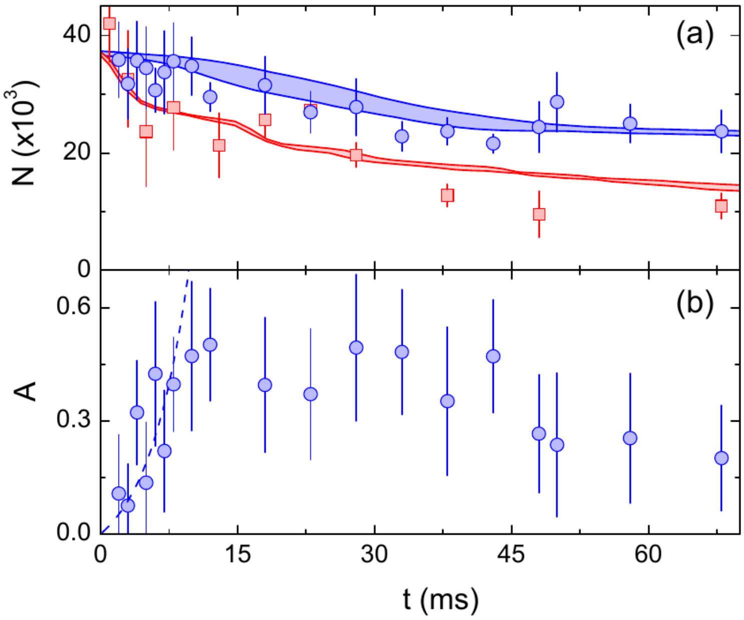

Figure 2.12: Panel (a): time evolution of atom number $N(t)$ for different values of the magnetic field B. In blue, $B = 5.279$ G and the system is in the stripe regime. In red, $B = 5.272$ G and the system is in the incoherent regime. Shaded areas correspond to atom loss predicted by simulations at the corresponding values of the scattering length a_s. Panel (b): time evolution of the interference amplitude A for $B = 5.279$ G, that is in the stripe regime. Initial growth for $t < 10$ ms fitted to an exponential (dashed line). Taken from [46].

At the same time, scientists in Pisa studied experimentally a very similar system and their results [46] turned out to be in agreement with the ones we have just discussed.

However, it is important to highlight that in both the experiments, the stripe supersolid phase has a short lifetime due to three-body losses: this is shown in Fig. 2.12. In the top panel, the time evolution of the atom number $N(t)$ shows an initial loss of particles on a timescale that is much shorter than the typical lifetime of a BEC, both in the stripe and the incoherent phase. The loss rate then decreases as the system reaches an incoherent or disorganized configuration. This is compatible with the evolution of the interference amplitude A in the bottom panel, which corresponds to the ratio between side peaks and center peak height in the interference pattern. It is characterized by an initial exponential growth during the formation of the density-modulated structure in the first 10 ms, it then remains stable until $t = 30$ ms and it finally decreases for longer times.

Therefore, only metastable stripe supersolid phases were observed in these experiments.

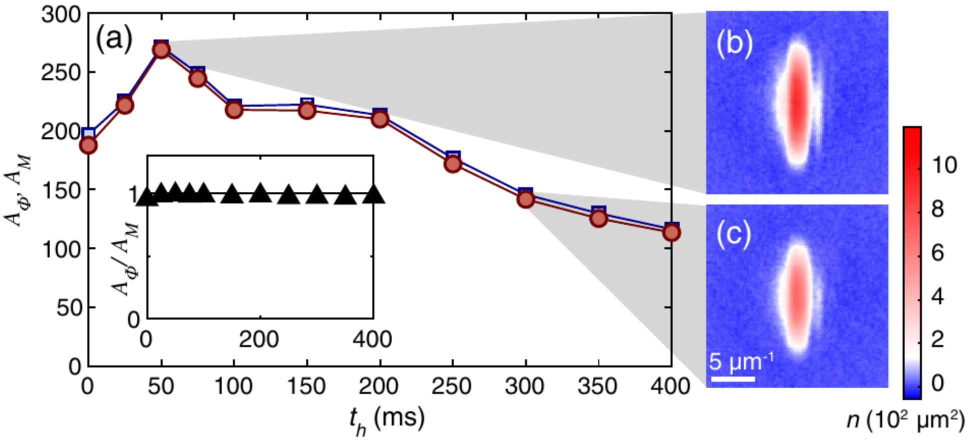

Figure 2.13: Panel (a): time evolution of amplitudes A_Φ (red circles) and $A_\mathcal{M}$ (blue squares) after evaporation time of 300 ms and equilibration time of 100 ms. Panels (b), (c): averaged absorption images of 25 realizations after 50 ms and 100 ms of holding time, respectively. The color map indicates the atomic density in momentum space. Taken from [59].

In Innsbruck instead, scientists were able to create a long-lived and robust supersolid [59]. They considered two different experimental setups, one with atoms of ^{166}Er and the other with ^{164}Dy. In the first case, they successfully realized a supersolid state, but with short lifetime similarly to the experiments we have already discussed, which had been performed with ^{162}Dy.

Interestingly, in the case of a BEC of ^{164}Dy the coherent density-modulated phase was remarkably long-lived and a lifetime longer than 150 ms was observed, as shown in Fig. 2.13. We can see that, after an equilibration time, both the amplitudes of frequency side peaks for the in-situ density modulation (A_Φ) and for the phase coherence ($A_\mathcal{M}$) decay slowly and the supersolid character is conserved for a longer time.

In 2021, the same group also successfully witnessed the formation of a supersolid state in a 2D geometry [61, 60]. In Fig. 2.14 we show an example of a state formed by an hexagon with a central droplet. The atoms are trapped as in panel (a) and then released from the trap to verify the presence of phase coherence, which is confirmed by the image averaged over many experimental trials in panel (b). Here, we see a clear density modulation in the interference pattern combined with a relevant degree of delocalization for particles, in agreement with the results of simulations of a phase-coherent state undergoing expansion, shown in panel (d).

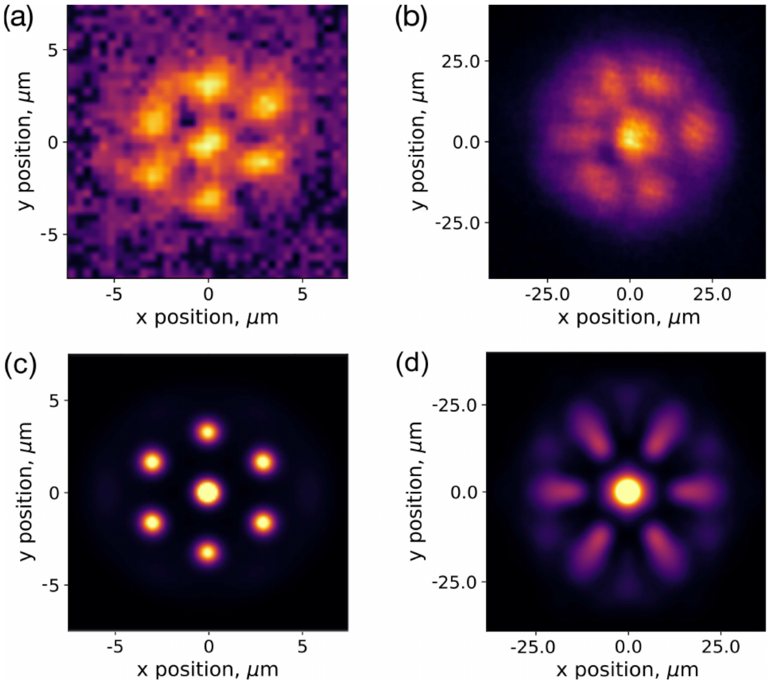

Figure 2.14: Experimental realization of seven droplet hexagon supersolid state. Panel (a): exemplary in-situ image of the density profile with trapped atoms. Panel (b): averaged image over 68 runs after time-of-flight expansion with atoms released from the trap. Panels (c), (d): corresponding simulations to panels (a) and (b), respectively. Taken from [60].

Before moving on, we want to highlight the fact that the works mentioned above considered mean-field regimes and high particle densities, which allow to describe

the systems under study by means of the famous (extended) Gross-Pitaevskii equation. This means that a semiclassical approach is implemented and quantum fluctuations are disregarded.
We will see that this path is not viable in our case, since quantum fluctuations are key to the emergence of interesting physics in our model, and this will lead us toward the use of computational techniques.

Chapter 3

Bose-Hubbard models and geometrical frustration

The much celebrated Bose-Hubbard model (BHM) and its variations represent the best tools to describe the physics of systems of ultracold bosonic atoms in discrete geometries. In this chapter we go through the main aspects of these models, restricting our review to the quasi-1D case, both for simplicity and because this is the most interesting frame for us.
In the second part instead, we introduce the concepts of geometrical frustration and chirality, which are fundamental features of the physical system we want to study.

3.1 Bose-Hubbard models

The Bose-Hubbard model has been first introduced by H. Gersch and G. Knollman [62] in 1963 with the aim of describing the physics of granular superconductors, where electrons couple forming the so-called Cooper pairs, which behave as bosonic quasiparticles. The model really gained the attention of many only a couple of decades later, thanks to the seminal paper by M. Fisher et al. [63], published in 1989. In fact, they noticed that the BHM was suitable for the description of the insulator-superfluid transition observed both in fermionic and bosonic systems. From that moment onward, this model attracted much interest and its full potential was understood, resulting in a great amount of studies on different situations and considering many variations of the basic model.

Let us start from the generic Hamiltonian of a weakly interacting gas of bosonic atoms in an optical lattice, written in the second quantization formalism [37]:

$$\begin{aligned} H = & \int d^3x \, \Psi^\dagger(\boldsymbol{x}) \left[\frac{\boldsymbol{p}^2}{2m} + V_0(\boldsymbol{x}) + V_T(\boldsymbol{x}) \right] \Psi(\boldsymbol{x}) \\ & + \frac{1}{2} \int d^3x \int d^3y \, \Psi^\dagger(\boldsymbol{x}) \Psi^\dagger(\boldsymbol{y}) \, g(|\boldsymbol{x}-\boldsymbol{y}|) \, \Psi(\boldsymbol{x}) \Psi(\boldsymbol{y}) \quad , \end{aligned} \tag{3.1}$$

where $\Psi(\boldsymbol{x})$ are the bosonic field operators, which satisfy the bosonic commutation rule $\left[\Psi(\boldsymbol{x}), \Psi^\dagger(\boldsymbol{y})\right] = \delta^3(\boldsymbol{x}-\boldsymbol{y})$. The field $V_0(\boldsymbol{x})$ is the potential that creates the optical lattice and has the form (2.3), while $V_T(\boldsymbol{x})$ is an external potential, which is needed in order to confine the atoms in the desired region of space. In the first term, we have a kinetic contribution with the momentum of a quantum particle $\boldsymbol{p} = -i\hbar\nabla$. The function $g(|\boldsymbol{x}-\boldsymbol{y}|)$ is the interaction strength between two atoms. We assume that only s-wave scattering between atoms in contact occurs, therefore obtaining $g(|\boldsymbol{x}-\boldsymbol{y}|) = \frac{4\pi a_s}{m}\delta^3(\boldsymbol{x}-\boldsymbol{y})$ with a_s the s-wave scattering length and m the mass of the atoms.

If we further assume that all the particles are in the lowest band of the optical lattice, we can expand the bosonic field operator in terms of Wannier functions $w_0(\boldsymbol{x})$. Therefore, we have: $\Psi(\boldsymbol{x}) = \sum_i b_i w_0(\boldsymbol{x}-\boldsymbol{x_i})$, where b_i is the annihilation operator for a boson at position $\boldsymbol{x_i}$. By performing the calculations, one finds the following model Hamiltonian:

$$H = -\sum_{i,j} J_{ij} b_i^\dagger b_j \; + \; \frac{1}{2} \sum_{i,j,k,l} U_{ijkl} b_i^\dagger b_j^\dagger b_k b_l \quad , \tag{3.2}$$

where we have position-dependent hopping coefficients

$$J_{ij} = -\int d^3x \, w_0(\boldsymbol{x}-\boldsymbol{x_i}) \left[\frac{\boldsymbol{p}^2}{2m} + V_0(\boldsymbol{x}) + V_T(\boldsymbol{x}) \right] w_0(\boldsymbol{x}-\boldsymbol{x_j})$$

and interaction coefficients

$$U_{ijkl} = g \int d^3x \, w_0(\boldsymbol{x}-\boldsymbol{x_i}) \, w_0(\boldsymbol{x}-\boldsymbol{x_j}) \, w_0(\boldsymbol{x}-\boldsymbol{x_k}) \, w_0(\boldsymbol{x}-\boldsymbol{x_l}) \quad .$$

In most of the cases, in particular for reasonably deep lattices V_0, the offsite interaction can be neglected and only terms U_{iiii} are kept. The same goes for hopping processes beyond nearest neighbor sites, so that one considers only terms $J_{i,i+1}$.

We now consider a trapping potential $V_T(\boldsymbol{x})$ that confines the particles in a quasi-1D cigar shaped geometry and we assume that the coefficients are independent of position, that is $U_{iiii} = U$, $J_{i,i+1} = t \; \forall i$. All this allows to reduce the model (3.2) to the following well-known Hamiltonian:

$$H = -t \sum_i \left(b_i^\dagger b_{i+1} + h.c. \right) \; + \; \frac{U}{2} \sum_i n_i (n_i - 1) - \mu \sum_i n_i \quad . \tag{3.3}$$

Here the index i runs over the sites of a 1D chain. The first term represents an hopping process between nearest neighbors with amplitude given by the coefficient t and *h.c.* stands for the hermitian conjugate of the product of operators $b_i^\dagger b_{i+1}$. This is a kinetic energy term, related to the delocalization of particles across the chain.
In the second term, U is the onsite interaction experienced by two bosons positioned at the same site and we have defined the number operator $n_i = b_i^\dagger b_i$. Finally, the last term determines the number of particles through the chemical potential μ, which is the energy penalty or bonus for adding a particle to the system, depending on its sign.

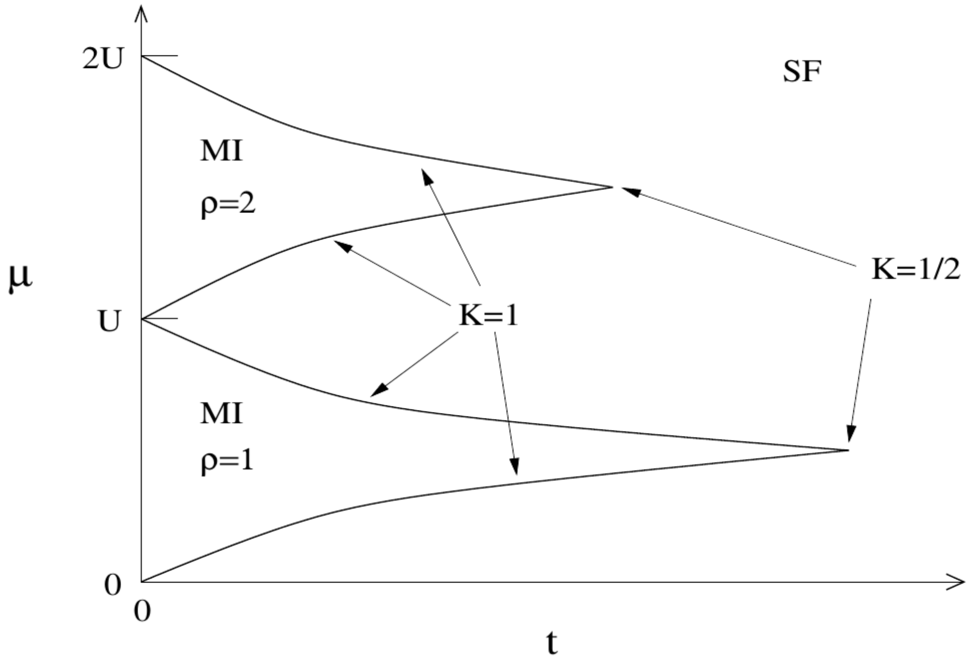

Figure 3.1: Schematic ground-state phase diagram of the 1D Bose-Hubbard model as a function of the chemical potential μ and the hopping amplitude t for fixed U. ρ is the number of particles per site, while K is the Luttinger parameter. Mott insulators (MI) at $\rho = 1$ and $\rho = 2$ are shown, outside the lobes the systems is in the superfluid (SF) phase. Taken from [64].

The ground-state phase diagram at zero temperature ($T = 0$) of the 1D BHM has been studied extensively both analytically and numerically [65, 66]. The phase diagram in the (t, μ) plane for fixed U is schematically shown in Fig. 3.1 [64].
As mentioned before, the parameter μ fixes the number of particles in the system and we see that an higher value of the chemical potential corresponds to higher

particle density, here indicated as ρ. The phase diagram presents two distinct phases: a Mott insulator (MI) and a superfluid (SF). Let us analyze the picture starting from the most simple limit, that is $t = 0$. In this case, the occupation of each site is determined by the condition that the onsite energy is minimized, where the latter can be written as:

$$\varepsilon\left(\rho\right) = -\mu\rho + \frac{U}{2}\rho\left(\rho - 1\right) \tag{3.4}$$

with $\rho \geq 1$. For any value of μ such that $\rho - 1 < \mu/U < \rho$, each site is occupied by ρ bosons. If instead we introduce a nonzero hopping amplitude $t > 0$, then the addition or removal of a particle brings a gain in kinetic energy, due to the additional particle or hole hopping from site to site. However, if t is not large enough, it is not possible to overcome the potential energy coming from the repulsive interaction between bosons on the same site: this is the case in the MI regions of Fig. 3.1. Therefore, for each integer value of the density ρ there exists a region where the number of particles per site is exactly ρ and each of them is confined in its site: thus, we have a Mott insulator. This phase is incompressible, since $\partial\rho/\partial\mu = 0$ and has an energy gap for the addition of a particle or a hole given by the distance in μ-direction from the upper or lower phase boundary, respectively. In such a phase, particles are localized and there is no phase coherence, as signaled by the exponential decay with distance of the expectation value $\langle b_i^\dagger b_j \rangle$.

These MI regions exhibit a characteristic lobe-like shape, which can be easily understood in terms of an energy balance. Indeed, for a fixed value of t, by approaching a phase boundary from within a lobe, the energy gap for the addition of particles or holes decreases. At the transition point, the kinetic energy gained through the hopping of extra particles or holes equals the energy penalty caused by the repulsive onsite interaction. At that point, the system undergoes a transition to a superfluid phase, where particles are delocalized and the average occupation of sites becomes non-integer. This SF phase is characterized by finite compressibility $\partial\rho/\partial\mu \neq 0$ and it is gapless with respect to particle/hole excitations.

As mentioned in Chapter 2, since we are working in the one-dimensional case, the continuous U(1) symmetry cannot be spontaneously broken and superfluidity is possible only for finite-size system. This is due to the power-law decay with distance of $\langle b_i^\dagger b_j \rangle$, which would still go to zero in the thermodynamic limit where $|i - j| \to \infty$.

The region of superfluidity extends around each lobe up to $t = 0$ at integer μ/U, because in that condition there is no difference in occupying sites with ρ or $\rho - 1$ particles, which means that the energy gap is zero.

The width of the lobes, namely the position of the tips in the t-direction, can be shown to approximately scale as $1/\rho$ for increasing ρ, thus displaying a hyperbolic behavior.

In the following, we will work in the microcanonical ensemble, that is at fixed number of particles in the system. In particular, we will consider $\mu = 0$ and omit the corresponding term from the equations. Therefore, we want to analyze how the system behaves when the density ρ is fixed to an integer value, say for instance $\rho = 1$, and the hopping amplitude t is varied for a fixed value of $U > 0$. This would be equivalent to approaching the tip of the lobe at fixed μ by increasing t. As in the previous case, at the tip, the gain in kinetic energy induced by the hopping of particles will be equal to the potential energy given by the onsite repulsion between bosons and a transition to a SF occurs. Nevertheless, in this case the average occupation of sites does not change, but particles are free to hop along the chain. Since we have a transition between a gapped and a gapless phase, it is interesting to consider the behavior of the charge gap, which is defined as:

$$\Delta E_C = E_{GS}\left(N-1,L\right) + E_{GS}\left(N+1,L\right) - 2E_{GS}\left(N,L\right) \quad , \tag{3.5}$$

where $E_{GS}\left(N,L\right)$ is the ground-state energy of the system with N particles and L sites. This is nothing but the algebraic sum between the energy difference in adding a particle, that is $E_{GS}\left(N+1,L\right) - E_{GS}\left(N,L\right)$, and a hole, namely $E_{GS}\left(N-1,L\right) - E_{GS}\left(N,L\right)$, to the chain.
In this frame, the model can be shown to belong to the universality class of the XY model, therefore the phase transition is of the Berezinskii-Kosterlitz-Thouless type [67, 68]. This kind of transition is characterized by a slow closing of the charge gap, in particular [64]:

$$\Delta E_C \sim exp\left(\frac{const.}{\sqrt{t_C - t}}\right) \tag{3.6}$$

with t_C the critical value of the hopping amplitude, at which the transition occurs. It is important to highlight the nature of this transition, because it implies that also the order parameters used to identify these two phases change smoothly and thus the width of the transition is quite large. We will see that something analogous is observed in our results (see Chapter 6).

A more accurate version of the ground-state phase diagram of the 1D BHM has been obtained in the following years thanks to the development of efficient simulation methods. An example of the phase-diagram produced with DMRG calculations [69] is shown in Fig. 3.2.

3.1.1 1D extended Bose-Hubbard model

We focus now on a variation of the BHM that includes also beyond-onsite interactions, namely the extended Bose-Hubbard model (EBHM). For this part of the work, we follow as a guide the article "*Phase diagram of the extended Bose Hubbard model*" by Davide Rossini and Rosario Fazio [70].

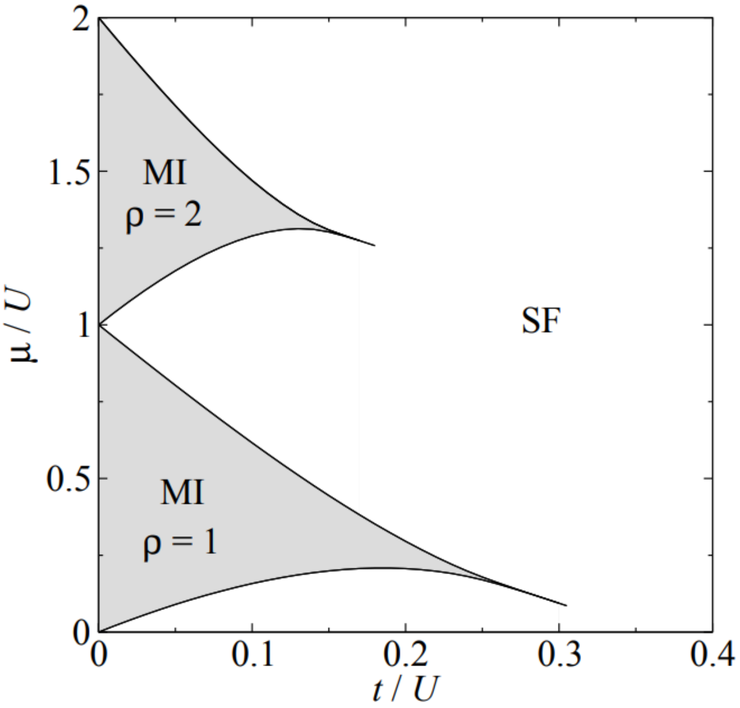

Figure 3.2: Schematic ground-state phase diagram of the 1D Bose-Hubbard model as a function of the chemical potential μ/U and the hopping amplitude t/U. ρ is the number of particles per site. Gray regions indicate Mott insulating (MI) phases, in white is the superfluid (SF) phase. Transition lines obtained with finite-size DMRG calculations. Taken from [69].

The EBHM has caught much attention in the last decades [71]. First of all, despite being the simplest model to include beyond-onsite interactions, it exhibits very interesting physics, as evidenced by the rich ground-state phase diagram in Fig. 3.3. On top of that, it is quite intuitive to extend the model to consider even longer-range interactions, e.g. dipolar interactions. Finally, the experimental platforms discussed in Chapter 2 are available for quantum simulation of this model and the level of complexity and controllability of these setups nowadays is extremely high.

The model Hamiltonian of the EBHM for a one-dimensional system is written as:

$$H = -\,t\sum_i \left(b_i^\dagger b_{i+1} + h.c.\right) + \frac{U}{2}\sum_i n_i\left(n_i - 1\right) + V\sum_i n_i n_{i+1} \;. \qquad (3.7)$$

With respect to Equation (3.3), here we have neglected the chemical potential term and we have an additional one containing a density-density interaction between

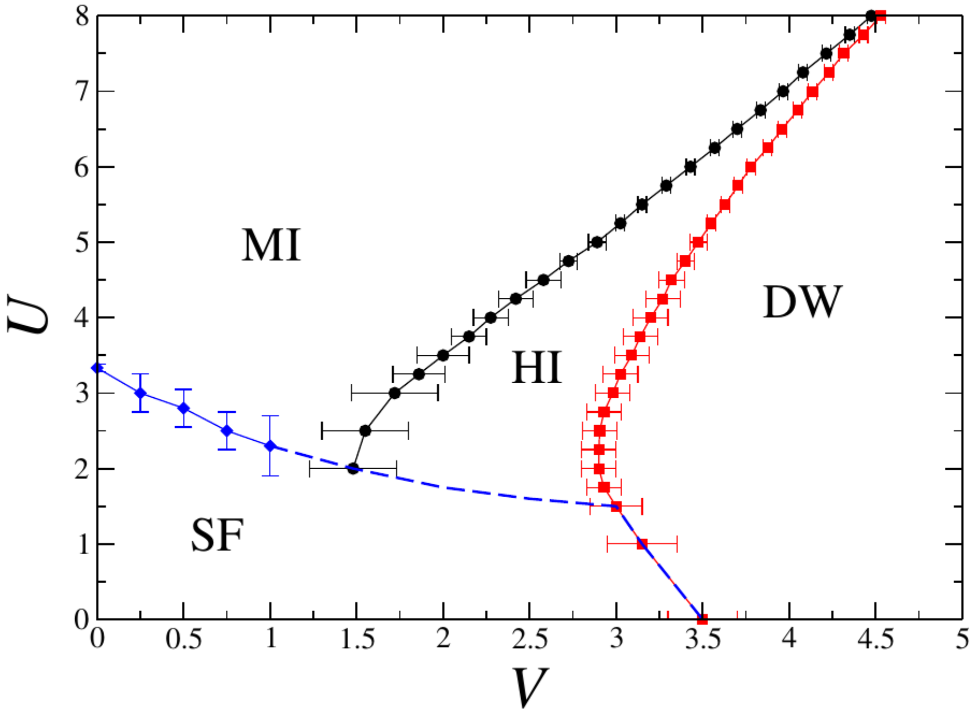

Figure 3.3: Ground-state phase diagram of the 1D EBHM in the (V, U) plane for fixed $t = 1$ at unit filling $\bar{n} = 1$. Phase boundaries obtained with finite-size DMRG calculations. The dashed blue line is an interpolation of the continuous blue curve and the red dots. Taken from [70].

nearest neighbors: the coefficient V is the value of the repulsion or attraction between two bosons located in adjacent sites of the chain.

In their paper, Rossini and Fazio considered the case of unit filling $\bar{n} = 1$, where the number of particles is equal to the number of sites in the chain, and they set the energy scale by fixing $t = 1$. As mentioned above, the ground-state phase diagram in this configuration, shown in Fig. 3.3, exhibits a rich variety of quantum phases. First of all, we recognize the Mott insulating and the superfluid phases that we already encountered and characterized in the simpler case of the BHM.

In addition to that, we find two more phases that arise due to presence of nearest neighbor interaction. In fact, there is a quantum phase transition (QPT) from the MI to an Haldane insulator (HI), which is a symmetry protected topological (SPT) phase characterized by an hidden order of the fluctuations of the local density [72]. Nevertheless, this phase does not break the translational symmetry of the lattice. Exactly at the transition point, the charge gap E_C (3.5) closes.

The second additional phase is a charge density wave, which can be observed for large values of the nearest neighbor repulsion V. This is reasonable because a sufficiently high value of such an interaction dominates over the kinetic energy and the onsite repulsion, freezing the system in a pattern of alternated occupied and empty sites. This gives the chain a density profile ... $-2-0-2-0-$ ..., since unit filling is considered. Notice that the charge gap is not able to capture the transition between the HI and the CDW, as it always stays finite across the phase boundary. Instead, the transition is reflected by the closing of another energy gap, the so-called neutral gap:

$$E_n = E_1\left(N, L\right) - E_{GS}\left(N, L\right) \quad , \tag{3.8}$$

where $E_1\left(N, L\right)$ is the energy of the first excited state of the system with N particles and L sites, so that the neutral gap is just the energy difference between the two lowest lying states in the energy spectrum.

In Chapter 5 we will extend this model by taking into account additional terms and we will see how this determines the emergence of even richer physics.

3.2 Geometrical frustration and chirality

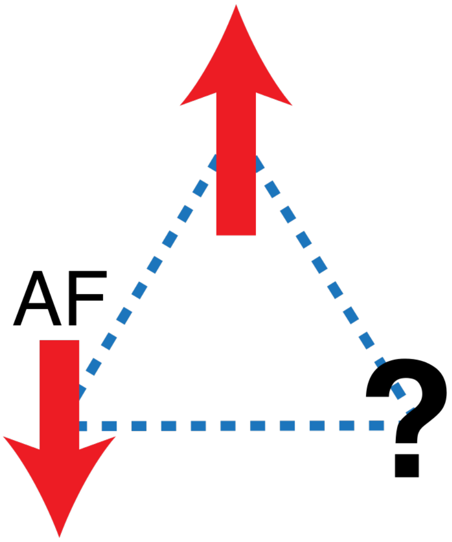

Figure 3.4: Example of geometrical frustration in the case of spins-1/2 with antiferromagnetic interaction on a triangular plaquette. The black question mark represents the degeneracy of the ground-state in the degree of freedom of the third spin, when the two red ones are already fixed to be antiparallel.

Geometrical frustration is a phenomenon related to the incompatibility between the properties of an interacting system and the geometrical disposition of its constituents, making it impossible to satisfy some physical constraint. In condensed matter physics, in particular in discrete systems, the phenomenon arises due to the interplay between conflicting interatomic forces on the lattice, that drive the system towards different configurations. In certain cases, this can lead to non-trivial and very exciting physics [73].

Frustration has been first considered for magnetic systems, starting from 1950 with the work by Wannier [74], while the term has been actually introduced only a couple of decades later by Toulouse [11]. Indeed, systems of spins provide probably the simplest example for the illustration of geometrical frustration and they exhibit a variety of exotic emergent phenomena, such as spin ice, spin glasses and spin liquid phases [73].
In general, spins with nearest neighbor couplings are described by a simple Hamiltonian:

$$H = J \sum_{\langle i,j \rangle} \mathbf{S}_i \cdot \mathbf{S}_j \ , \tag{3.9}$$

with $J < 0$ in the case of ferromagnetic interaction and $J > 0$ for antiferromagnetic interaction. Here, $\mathbf{S}_i$ is the spin operator for a spin in position i and $\langle i, j \rangle$ denotes the sum over nearest neighbor pairs.

Now, let us consider three antiferromagnetic spins-1/2 positioned on a plaquette of a triangular lattice, as shown in Fig. 3.4. Since antiferromagnetic interaction favors antiparallel spins, in the ground-state each spin would like to be antiparallel to its two neighbors. However, it is immediately evident that this is not possible with such a geometry. In fact, if we suppose that we have fixed the two red spins in Fig. 3.4, the third one is simultaneously pushed towards opposite directions by them and this leads to the emergence of a degeneracy in the configuration of the ground-state.
This degeneracy can be much higher if one considers spins with more degrees of freedom, for instance Heisenberg vector spins, and other complex lattices, such as the kagome or the pyrochlore ones [73].

Focusing on the one-dimensional case, frustrated magnets have been subjected to intensive theoretical and experimental research, leading to the discovery of novel quantum states, such as topological insulators and superconductors [75], quantum spin liquids [76] and valence bond solids [77, 78]. The most interesting phenomenon to us is the emergence of chiral phases [79].
Chirality is a property present in many branches of science and it is related to the breaking of a left-right symmetry that causes a system or a phenomenon not to be identical to its mirror image. One of the most renowned example is provided by

chemistry, where some molecules are not superposable to their mirror image: the two mirror images of a chiral molecule are called enantiomers.

In the case of spin-1/2 frustrated chains, chirality arises as the consequence of the breaking of a $\mathbb{Z}_2$ symmetry, more precisely the time-reversal symmetry. In particular, this is signaled by a non-vanishing and uniform value of the vector chirality, defined as:

$$k_i^z = \langle (\mathbf{S}_i \times \mathbf{S}_{i+1})^z \rangle \ . \tag{3.10}$$

Within physics, chirality plays a major role in condensed matter theory as chiral properties are often present in edge theories [80].
Furthermore, it is an important element in high energy physics, in particular in the standard model of particles. For instance, the studies on neutrinos observed that all neutrinos are left-handed, while antineutrinos are right-handed [81].
Another fact is represented by charged weak interactions among fermions: only left-handed ones interact among them, while right-handed fermions are excluded from interaction among them and with left-handed ones [82]. This parity violation has been first confirmed in the famous Wu experiment in the 1950s [83].
There have been also efforts to develop consistent chiral lattice gauge theories [84].
From a more applicative point of view, chirality can also provide interesting opportunities in quantum information theory, for instance allowing to design non-reciprocal circuits in the context of chiral quantum spintronics [85].
All of this makes the discovery and realization of chiral phases and the study of their properties a very important task.

Chapter 4

Simulation methods

Many interesting models for bosons, both in the continuum and in lattices, are not exactly solvable and, in general, it may be extremely difficult to extract any information by means of analytical tools [86]. This is particularly true in the case of low-dimensional systems at relatively low densities, where quantum fluctuations play a fundamental role in determining the physics that emerges. As we have seen in Chapter 3, in the case of the (e)BHM fluctuations are encoded in the hopping term, whose presence allows for the observation of non-trivial physics.
A possible approach is to focus on the low-energy properties of the models, adopting some assumptions that simplify the calculations. However, in many cases the most exciting physics is observed in deeply quantum regimes, where analytical approaches fail to deliver reliable results.
Therefore, one needs to resort to computational techniques, as some of them turned out to be very powerful in simulating strongly correlated systems.
Focusing on our case of interest, that is bosons in a one-dimensional lattice, there are some methods available, such as the Quantum Monte Carlo (QMC) algorithm [87] and the stochastic series expansion (SSE) algorithm [88], but the most renowned and powerful ones are represented by exact diagonalization and Density Matrix Renormalization Group (DMRG).

Indeed, exact diagonalization is the most straightforward approach and we could call it the “brute force” technique. It consists in writing the Hamiltonian of a finite system in a suitable basis and diagonalizing it: the eigenvalues and eigenvectors obtained allows to compute any physical observable. For instance, if we choose the site basis $\{|i\rangle\}$, a basis state for a lattice with L sites is written as:

$$|m\rangle = |i_1\rangle \otimes |i_2\rangle \otimes ... \otimes |i_L\rangle \quad . \tag{4.1}$$

From this, one can readily compute the Hamiltonian matrix. However, we immediately notice that this method is strongly limited by the number of states p in the

chosen basis: the size of the Hilbert space increases exponentially with the number of basis vectors. In the case of the site basis, the dimension of the matrix that has to be diagonalized is $p^L \times p^L$. This may be acceptable in the case of hard-core bosons where $p = 2$, since a site can be either empty $|0\rangle$ or occupied by a single boson $|1\rangle$, but it becomes unfeasible in the case of soft-core bosons where p has to be quite large, and should in principle be infinite.
This limitation is overcome by the famous DMRG algorithm, that we present extensively in the following section, since we exploit it for simulating the model under study, which will be introduced later in Chapter 5.

4.1 Density Matrix Renormalization Group

The Density Matrix Renormalization Group algorithm has been first proposed in 1992 by Steven White [89, 90] for the identification of the ground-state and first excited states of strongly correlated quantum systems in one dimension. Here we review the main aspects of this algorithm and the extensions developed since its invention, referring mainly to the reviews by De Chiara et al. [91], Schöllwock [92] and Orús [93].

In the initial formulation by White, DMRG was inspired by Wilson's Numerical Renormalization Group (NRG), which is the simplest way to perform real-space renormalization of Hamiltonians. This method had been developed by Wilson in the 1970s in attempts to solve the so-called Kondo problem [94, 95], dealing with a non-monotonic behavior of resistivity in metals with a small amount of magnetic impurities. The starting point consists in a small part of a quantum system, in particular we consider a block $\mathcal{B}$ of size L in a m-dimensional Hilbert space, and a Hamiltonian that describes the interaction between two such blocks. The composite 2-block system, now represented in dimension m^2 is projected onto the subspace spanned by the m lowest lying energy eigenstates: this returns a new truncated representation in dimension m and all operators are also projected onto this new basis. Then, the system size is increased and the procedure is repeated iteratively, until one reaches the full size of the system. However, this procedure fails for strongly correlated systems, because the decimation of the Hilbert space is based on the assumption that the ground-state of the full system is composed of low-lying states of smaller subsystems: this is true only is selected cases.

White was able to go beyond this limitation by embedding the block in an environment that mimics the thermodynamic limit of the system before the decimation takes place; unfortunately, this implies a slowdown of the algorithm.

4.1.1 Infinite DMRG

Let us start with the description of the infinite version of the algorithm, called iDMRG. Starting from an initial unit cell, this method considers chains of increasing length, at each iteration discarding a sufficient number of states to keep the size of the Hilbert space under control. There are two key assumptions: a reduced state space that describes well the relevant physics of the system exists and we can devise a procedure to identify it, which is the crucial point of the theory.

Let us write a generic system Hamiltonian as:

$$H = \sum_i \sum_q \left[J\left(q\right) S_i\left(q\right) T_{i+1}\left(q\right) + B\left(q\right) V_i\left(q\right) \right] \quad , \tag{4.2}$$

where $J\left(q\right)$ and $B\left(q\right)$ are coupling constants and $\left\{S_i\left(q\right)\right\}_q$, $\left\{T_i\left(q\right)\right\}_q$ and $\left\{V_i\left(q\right)\right\}_q$ are sets of operator acting on site i, while the index q runs over the elements of the sets. In the following, we are going to use the notation $\mathcal{B}\left(L, m_L\right)$ to denote a block of L sites described with m_L states.

We start with a block with a single site $\mathcal{B}\left(1, p\right)$, where p is the number of possible states for a site, and we add another site to the right, creating the so-called left enlarged block, whose Hamiltonian is:

$$H_E = H_B + H_S + H_{BS} \tag{4.3}$$

with H_B the local Hamiltonian of the block, H_S the local Hamiltonian of the site and H_{BS} the interaction term between the two. We can now build the corresponding right enlarged block analogously with Hamiltonian $H_{E'}$ and consider also the interaction between the two enlarged blocks: we thus obtain a superblock that describes the whole system. Its Hamiltonian is written as:

$$H_{supB} = H_E + H_{E'} + H_{SS'} \quad , \tag{4.4}$$

where $H_{SS'}$ is the interaction term between the two free sites that connect the enlarged blocks. The ground-state is now obtained by diagonalizing H_{supB}:

$$\left|\psi_{GS}\right\rangle = \Psi_{a\alpha\beta b} \left|a\alpha\beta b\right\rangle \quad , \tag{4.5}$$

with Latin letters denoting blocks and Greek ones free sites. Notice that it is possible to extract the ground-state of the superblock without finding the full spectrum: this can be achieved by exploiting efficient numerical diagonalization methods, such as the Lanczos algorithm [96, 97].

The reduced density matrix ρ_L of the left enlarged block is obtained as the trace over the degrees of freedom of the right enlarged block:

$$\rho_L = \mathrm{Tr}_R \left|\psi_{GS}\right\rangle \left\langle\psi_{GS}\right| = \Psi_{a\alpha\beta b} \Psi^*_{a'\alpha'\beta b} \left|a\alpha\right\rangle \left\langle a'\alpha'\right| \quad . \tag{4.6}$$

The renormalization step of the algorithm is made at this stage, by truncating the Hilbert space of the enlarged block in order to represent it in a basis with at most D elements, with the threshold D called bond dimension (BD) and fixed a priori. Therefore, the Hilbert space takes dimension $m_{L+1} = \min\left(m_L p, D\right)$ and it is composed by the first m_{L+1} eigenstates of the reduced density matrix ρ_L, which are associated to the largest eigenvalues. In more mathematical terms, the truncated change of basis is performed by introducing a transfer matrix $O_{L\to L+1}$ of dimension $m_L p \times m_{L+1}$: the columns of this matrix corresponds to the m_{L+1} eigenstates that we want to keep. We get a truncated enlarged block $\mathcal{B}\left(L+1, m_{L+1}\right)$ with Hamiltonian:

$$H'_B = O^{\dagger}_{L\to L+1}\, H_E\, O_{L\to L+1} \ , \tag{4.7}$$

while the local operators are transformed as:

$$S'_{L+1}\left(q\right) = O^{\dagger}_{L\to L+1}\, S_{L+1}\left(q\right)\, O_{L\to L+1} \tag{4.8}$$

and similarly for $T'_{L+1}\left(q\right)$ and $V'_{L+1}\left(q\right)$. This procedure can be repeated iteratively, increasing the size of the system by 2 sites at each step and making it closer and closer to the ideal thermodynamic limit, until some convergence criterion for the observables is fulfilled. As the system gets bigger, the number of states used to describe it does not change and thus the computational complexity of the problem is fixed a priori by the values of D and p.

At each iteration we introduce a truncation error that corresponds to the sum of the discarded eigenvalues of ρ_L:

$$\epsilon_{tr} = \sum_{i>D} \lambda_i \ . \tag{4.9}$$

Therefore, one needs to find a good trade-off between computational time and precision, identifying a suitable value for the bond dimension D, that must be small enough to make the calculation feasible but also large enough to capture the relevant physics of the system under study.

A schematic visualization of a single iDMRG step is presented in Fig. 4.1(a).

4.1.2 Finite-size DMRG

In many cases, iDMRG is not able to produce sufficiently accurate results. The finite-size version of the algorithm can be useful to reach better precision in the simulation of systems in complex configurations, for instance close to a first-order transition.

In this method, the infinite algorithm works as explained above, but it is stopped at a predetermined length of the system L_{max} and once this value is reached, the following DMRG steps are slightly modified. In particular, at this point the system

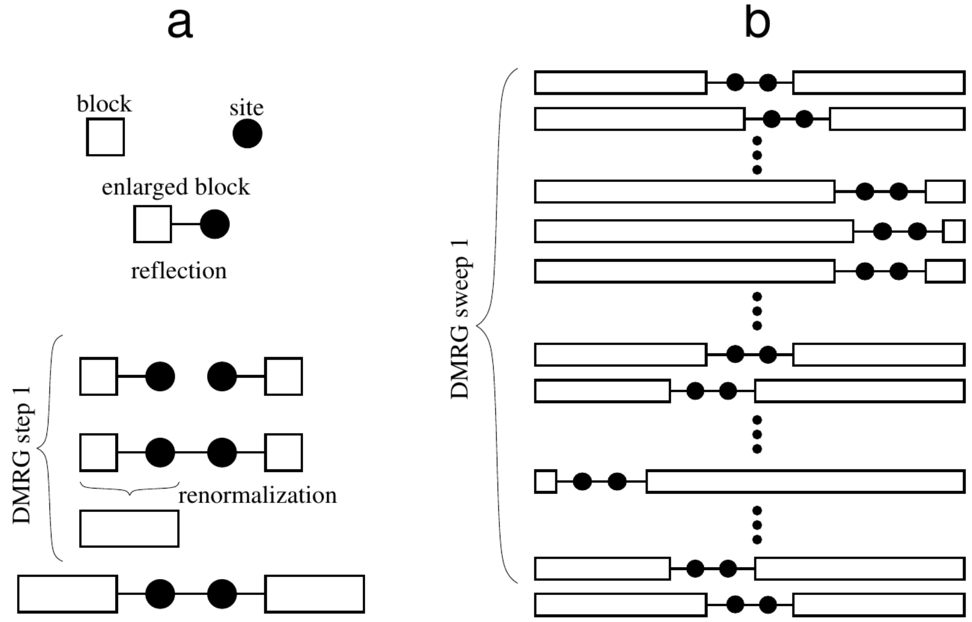

Figure 4.1: Schematic representation of DMRG. Left, panel **a**: one iteration of the iDMRG algorithm. Right, panel **b**: one full finite-size DMRG sweep. Taken from [91].

is formed by two blocks $\mathcal{B}\left(L_{max}/2-1\right)$ and two adjacent free sites, see the first row of Fig. 4.1(b). Now only the left block is enlarged, while the right one gets shrunk so that the size of the superblock is kept fixed at L_{max}. Therefore, now the system is formed by $\mathcal{B}\left(L_{max}/2\right)$ and $\mathcal{B}\left(L_{max}/2-2\right)$ with two free sites in the middle. The reduced basis transformations are performed only for the growing block, since the right block can be recovered from memory if one appropriately saves the transfer matrices, the block Hamiltonians and the local operators obtained in the previous steps.
This procedure is repeated until the right block is simply $\mathcal{B}\left(1,p\right)$, that is a single site: at this point, the role of the two blocks is exchanged and the right block starts to be grown, until the left boundary of the chain is reached. There, the left block is enlarged again at expenses of the right one, till the initial configuration is recovered: one full DMRG sweep has been completed, as shown in Fig. 4.1(b).
After each sweep, the approximation of the ground-state improves and the algorithm stops when the convergence criterion is fulfilled.

As is evident from Fig. 4.1, this algorithm describes systems with open boundary conditions (OBC). Periodic boundary conditions (PBC) can still be implemented, but in general DMRG favors OBC.

Let us mention the fact that a variation of this algorithm called t-DMRG has been developed for considering time-evolving systems. Starting from the output of a finite-size DMRG run, the time evolution of the ground-state is performed by exploiting a Suzuki-Trotter decomposition [98, 99] of the time evolution operator $U = e^{-iH_1 t}$, where H_1 is the Hamiltonian determining the dynamics of the system. However, the error introduced by this procedure is usually quite relevant and it increases with time, so the reliability of the algorithm is limited to quite short time intervals [100].

Area law for the entanglement entropy

Let us consider more deeply the quality of the approximate results provided by DMRG and explain why this algorithm works so well for one-dimensional systems. Since we are truncating the reduced density matrix, the amount of information that is lost is quantified by Equation (4.9). Therefore, it is important to understand how quickly the eigenvalues of the matrix decrease. This has been computed for some exactly solved systems both in 1D and 2D [101, 102, 103], showing that one-dimensional gapped systems exhibit an exponentially fast decay of the eigenvalues, while in 2D stripes of size $L \times W$ with $L \gg W$ the rate of decay is inversely proportional to W, so it gets slower as the two-dimensional character of the system is increased. Thus, it is clear why 1D systems are much preferable with respect to 2D ones for DMRG analysis.

For a generic system though, we don't know how the eigenvalue spectrum behaves. However, the entanglement entropy (von Neumann entanglement) comes in handy, as it is given by the non-vanishing part of the spectrum of the reduced density matrix ρ_A for a bipartitioning A|B of the system under study:

$$S_{A|B} = -\mathrm{Tr}\rho_A \log_2 \rho_A = -\sum_i \lambda_i \log_2 \lambda_i \ . \tag{4.10}$$

Indeed, we can extract the scaling of this quantity thanks to the so-called area laws [104]. If partition A has size $L^{\mathcal{D}}$ with $\mathcal{D}$ the spatial dimension, the area laws predict that, while thermal entropy is extensive, entanglement entropy of gapped ground-states of short-ranged Hamiltonians is proportional to the "surface" of the partition:

$$S_{A|B} \sim L^{\mathcal{D}-1} \ . \tag{4.11}$$

Therefore, for $\mathcal{D} = 1$ we have $S \sim const$, whereas $S \sim L$ in the two-dimensional case. Note that this is valid sufficiently far from critical points, where instead things are much more complex.

This can be intuitively connected to DMRG, where we deal with two D-dimensional state spaces for the partitions A and B: the maximal entanglement occurs when all eigenvalues of ρ_A are identical and in particular equal to D^{-1}, yielding $S_{A|B} = \log_2 D$. Then, one needs a state of dimension 2^S and more to describe the entanglement properly. Thus, for gapped systems in one dimension increasing the system size does not lead to a strong increase in the value of the bond dimension D since $S \sim const$, while in two dimensions D grows as 2^L because $S \sim L$ and DMRG fails even for relatively small systems.
In addition to that, note that in most cases, far enough from phase transitions, the eigenvalue spectrum is not flat but it usually decays exponentially: therefore, the worst case scenario depicted above does not occur in many occasions.

4.1.3 Tensor Networks

A few years after the algorithm was originally developed by White, thanks to the works by Vidal, Cirac and Verstraete among others [105, 106, 107, 108, 109], it was realized that the relevant corner of the Hilbert space can be parametrized efficiently by means of tensor networks (TN), which allows for a beautiful and intuitive formalization of DMRG and also other similar methods. As entailed by their name, tensor network methods represent quantum states in terms of networks of interconnected tensors, which capture the relevant entanglement properties of the system under study, providing a graphical language for condensed matter physics. In particular, two types of networks are used: Matrix Product States (MPS) for 1D systems and Projected Entangled Product States (PEPS) for 2D systems [93], see Fig. 4.2. Since here we are interested in the one-dimensional case, the focus of our discussion is on MPS methods.

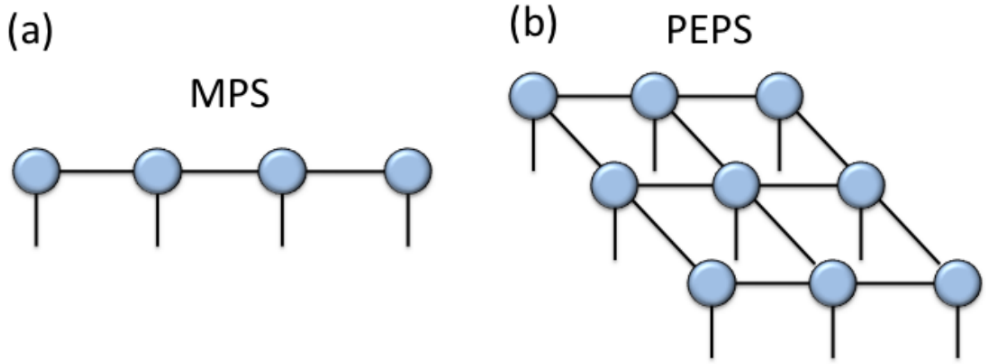

Figure 4.2: Examples of tensor network diagrams. Panel (a): MPS for 4 sites with OBC. Panel (b): PEPS for a 3×3 lattice with OBC. Taken from [93].

In general, a tensor is a multidimensional array of complex numbers and its rank is given by the number of indices. In the following, we will make use of index contraction, which is the sum over all the possible values of the repeated indices of a set of tensors. Indeed, a tensor network is a set of tensors with some of their indices contracted according to a certain pattern. A simple example is given by the scalar product of two vectors:

$$C = \sum_{\alpha=1}^{D} A_\alpha B_\alpha \ , \tag{4.12}$$

where C is just a complex number, that is a rank-0 tensor. In the diagrammatic representation of Fig. 4.2, blue circles are tensors, whereas the black lines sticking out from them correspond to the indices and we talk about "legs" of a tensor. Note that connected legs indicate index contraction, while free legs represent open indices. As we will see in the following, this graphical notation makes calculations much easier to handle.

It is important to highlight that the order in which the contraction is performed heavily influences the computational cost of the operation: finding the optimal order is key for the development of an efficient implementation of TN methods.

Let us see how an arbitrary quantum state can be translated into a Matrix Product State by means of a singular value decomposition (SVD). Note that in many cases this can be achieved with the simpler QR decomposition, which is numerically cheaper.

MPS are tensor networks that correspond to a 1D array of tensors, as can be seen in Fig. 4.2(a), and this is the reason why they are suitable for the description of one-dimensional systems. We consider a quantum many-body system of L sites, each of these having degrees of freedom described by p states. The corresponding wavefunction can be written as:

$$|\psi\rangle = \sum_{i_1,i_2,\ldots,i_L} C_{i_1 i_2 \ldots i_L} |i_1\rangle \otimes |i_2\rangle \otimes \cdots \otimes |i_L\rangle \tag{4.13}$$

for the local basis $|i_r\rangle$, $r = 1, ..., L$. Here, $C_{i_1 i_2 \ldots i_L}$ are p^L complex numbers and they are the coefficients of a tensor C with L indices $i_r = 1, ..., p$ for each site r. The total number of coefficients is $O\left(p^L\right)$, thus the amount of parameters describing the wavefunction in (4.13) scales exponentially with the size of the system. We want to decompose the large tensor C with a TN made by tensors of smaller rank, looking for a representation of the wavefunction in terms of a polynomial number of parameters.

The first step consists in reshaping the state vector with p^L components into a matrix Ψ of dimension $p \times p^{L-1}$ and then perform an SVD of this new matrix:

$$C_{i_1 \ldots i_L} = \Psi_{i_1,(i_2 \ldots i_L)} = \sum_{a_1}^{r_1} U_{i_1,a_1} S_{a_1,a_1} V^{\dagger}_{a_1,(i_2 \ldots i_L)} = \sum_{a_1}^{r_1} U_{i_1,a_1} C_{a_1 i_2 \ldots i_L} \ , \tag{4.14}$$

where $C_{a_1 i_2 \ldots i_L}$ is obtained by carrying out the product between S and $V^{\dagger}$ and reshaping it into a vector. Here and in the following, the i's are the site indices and the a's are the bond indices. The key condition for the reduction of the complexity of the problem is on the rank: $r_1 \leq p$. The matrix U is now decomposed into p row vectors A^{i_1} with $A^{i_1}_{a_1} = U_{i_1,a_1}$, while instead $C_{a_1 i_2 \ldots i_L}$ is reshaped into a matrix $\Psi_{(a_1 i_2),(i_3 \ldots i_L)}$ of dimension $r_1 p \times p^{L-2}$. This returns:

$$C_{i_1 \ldots i_L} = \sum_{a_1}^{r_1} A^{i_1}_{a_1} \Psi_{(a_1 i_2),(i_3 \ldots i_L)} \ . \tag{4.15}$$

The procedure is repeated iteratively for the matrix $\Psi_{(a_1 i_2),(i_3 \ldots i_L)}$ under the condition $r_2 \leq r_1 p \leq p^2$ and so on. In the end, one gets:

$$C_{i_1 \ldots i_L} = \sum_{a_1,\ldots,a_{L-1}} A^{i_1}_{a_1} A^{i_2}_{a_1,a_2} \cdots A^{i_{L-1}}_{a_{L-2},a_{L-1}} A^{i_L}_{a_{L-1}} = A^{i_1} A^{i_2} \cdots A^{i_{L-1}} A^{i_L} \ , \tag{4.16}$$

which allows us to write the quantum state in the form of a left-canonical MPS:

$$|\psi\rangle = \sum_{i_1,\ldots,i_L} A^{i_1} A^{i_2} \cdots A^{i_{L-1}} A^{i_L} |i_1\rangle \otimes |i_2\rangle \otimes \cdots \otimes |i_L\rangle \ . \tag{4.17}$$

By recalling the properties of SVD, it can be shown that the matrices A are left-normalized, that is:

$$\sum_{i_r} A^{i_r \dagger} A^{i_r} = I \ , \tag{4.18}$$

where I represents the identity matrix.
Since in DMRG we have a bipartitioning of the system in two blocks A and B, it is useful to introduce the following states:

$$|a_l\rangle_A = \sum_{i_1,\ldots,i_l} \left(A^{i_1} A^{i_2} \cdots A^{i_l} \right)_{1,a_l} |i_1\rangle \otimes \cdots \otimes |i_l\rangle \ , \tag{4.19}$$

$$|a_l\rangle_B = \sum_{i_{l+1},\ldots,i_L} \left(A^{i_{l+1}} A^{i_{l+2}} \cdots A^{i_L} \right)_{a_l,1} |i_{l+1}\rangle \otimes \cdots \otimes |i_L\rangle \ , \tag{4.20}$$

such that the MPS can be written as:

$$|\psi\rangle = \sum_{a_l} |a_l\rangle_A |a_l\rangle_B \ . \tag{4.21}$$

Due to the left-normality of A matrices, the states $\{|a_l\rangle_A\}$ form an orthonormal set:

$$ {}_A\langle a'_l|a_l\rangle_A = \delta_{a'_l,a_l} \ \ , \tag{4.22}$$

while in general this is not true for the states $\{|a_l\rangle_B\}$.

After the first SVD in (4.14), the whole procedure can be performed also in the opposite direction by reshaping $V^\dagger$ in column vectors and carrying out the product between U and S, finally obtaining a right-canonical MPS:

$$|\psi\rangle = \sum_{i_1,\ldots,i_L} B^{i_1}B^{i_2}\cdots B^{i_{L-1}}B^{i_L}\,|i_1\rangle\otimes|i_2\rangle\otimes\cdots\otimes|i_L\rangle \ \ , \tag{4.23}$$

with right-normalized B matrices:

$$\sum_{i_r} B^{i_r}B^{i_r\dagger} = I \ \ . \tag{4.24}$$

The MPS can be written again as in (4.21) by replacing A matrices with B matrices in (4.19) and (4.20), so that this time the states $\{|a_l\rangle_B\}$ form an orthonormal set, whereas in general $\{|a_l\rangle_A\}$ do not.

It is extremely convenient to mix the decomposition from the two sides in order to obtain an MPS in the so-called mixed canonical form. Let us assume that we have the following decomposition from the left up to a certain site l:

$$C_{i_1\ldots i_L} = \sum_{a_l}\left(A^{i_1}\cdots A^{i_l}\right)_{a_l} S_{a_l,a_l}V^\dagger_{a_l,(i_{l+1}\ldots i_L)} \ \ . \tag{4.25}$$

We can now reshape $V^\dagger_{a_l,(i_{l+1}\ldots i_L)}$ as $\Psi_{(a_l i_{l+1}\ldots i_{L-1}),i_L}$ and decompose from the right until we reach site i_{l+2}. In the last step, we are left with $U_{(a_l i_{l+1}),a_{l+1}}S_{a_{l+1},a_{l+1}}$ and we reshape it into $B^{i_{l+1}}_{a_l a_{l+1}}$, so that:

$$V^\dagger_{a_l,(i_{l+1}\ldots i_L)} = \sum_{a_{l+1},\ldots,a_{L-1}} B^{i_{l+1}}_{a_l,a_{l+1}}\cdots B^{i_L}_{a_{L-1}} \tag{4.26}$$

with right-normalized B matrices. Therefore, we obtain:

$$C_{i_1\ldots i_L} = A^{i_1}\cdots A^{i_l}\,S\,B^{i_{l+1}}\cdots B^{i_L} \ \ , \tag{4.27}$$

containing the singular values on the bond $(l, l+1)$.
Now, if we denote $\lambda_{a_l} = S_{a_l,a_l}$ and we introduce the states:

$$|a_l\rangle_A = \sum_{i_1,\ldots,i_l}\left(A^{i_1}A^{i_2}\cdots A^{i_l}\right)_{1,a_l}|i_1\rangle\otimes\cdots\otimes|i_l\rangle \ \ , \tag{4.28}$$

$$|a_l\rangle_B = \sum_{i_{l+1},\dots,i_L} \left(B^{i_{l+1}} B^{i_{l+2}} \cdots B^{i_L}\right)_{a_l,1} |i_{l+1}\rangle \otimes \cdots \otimes |i_L\rangle \quad , \tag{4.29}$$

we can finally write:

$$|\psi\rangle = \sum_{a_l} \lambda_{a_l} |a_l\rangle_A |a_l\rangle_B \quad . \tag{4.30}$$

Equation (4.30) is exactly the Schmidt decomposition of the quantum state, because both the states belonging to A and B, that we call Schimdt vectors, form orthonormal sets.

In order to connect this more directly to DMRG, let us perform a change of basis from the Schmidt basis back to the local one for a system of L sites [105, 106]. We start with a Schimdt decomposition between site 1 and the other $L-1$ sites and consider a bond dimension D:

$$|\psi\rangle = \sum_{a_1=1}^{min(p,D)} \lambda_{a_1} |a_1\rangle_A |a_1\rangle_B \quad , \tag{4.31}$$

where $\lambda^{[1]}_{a_1}$ are the Schimdt coefficients, while $|a_1\rangle_A$ and $|a_1\rangle_B$ are the left and right Schimdt vectors, respectively. We can now rewrite the left vector in terms of the local basis $|i_1\rangle$, so that:

$$|\psi\rangle = \sum_{i_1=1}^{p} \sum_{a_1=1}^{min(p,D)} \Gamma^{i_1}_{a_1} \lambda_{a_1} |i_1\rangle \otimes |a_1\rangle_B \quad , \tag{4.32}$$

where $\Gamma^{i_1}_{a_1}$ comes from the change of basis $|a_1\rangle_A = \sum_{i_1} \Gamma^{i_1}_{a_1} |i_1\rangle$. The procedure can be repeated for the second site from the left, leading to:

$$|\psi\rangle = \sum_{i_1,i_2=1}^{p} \sum_{a_1=1}^{min(p,D)} \sum_{a_2=1}^{min\left(p^2,D\right)} \left(\Gamma^{i_1}_{a_1} \lambda_{a_1} \Gamma^{i_2}_{a_1 a_2} \lambda_{a_2}\right) |i_1\rangle \otimes |i_2\rangle \otimes |a_2\rangle_B \quad . \tag{4.33}$$

By iterating this for the entire chain, we end up with:

$$|\psi\rangle = \sum_{\{i\}} \sum_{\{a\}} \left(\Gamma^{i_1}_{a_1} \lambda_{a_1} \Gamma^{i_2}_{a_1 a_2} \lambda_{a_2} \cdots \lambda_{a_{L-1}} \Gamma^{i_L}_{a_{L-1}}\right) |i_1\rangle \otimes |i_2\rangle \otimes \cdots \otimes |i_L\rangle \quad , \tag{4.34}$$

where we see a new clean decomposition for the coefficients of the tensor C:

$$C_{i_1 i_2 \dots i_L} = \Gamma^{i_1}_{a_1} \lambda_{a_1} \Gamma^{i_2}_{a_1 a_2} \lambda_{a_2} \cdots \lambda_{a_{L-1}} \Gamma^{i_L}_{a_{L-1}} \quad . \tag{4.35}$$

This canonical form can be obtained also for an infinite MPS [107] and it will be formed by as much tensors Γ and vectors λ as the number of sites in the unit cell of the state. An example of both finite and infinite MPS in canonical form is shown

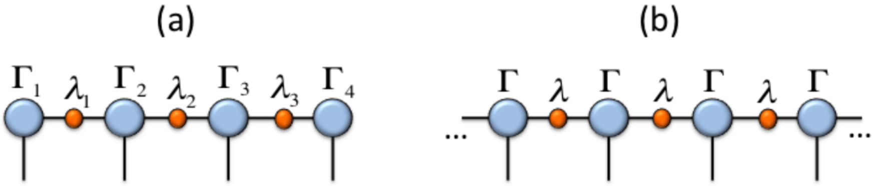

Figure 4.3: Examples of MPS in canonical form. Panel (a): finite MPS with 4 sites. Panel (b): fnfinite MPS with single-site unit cell. Taken from [93].

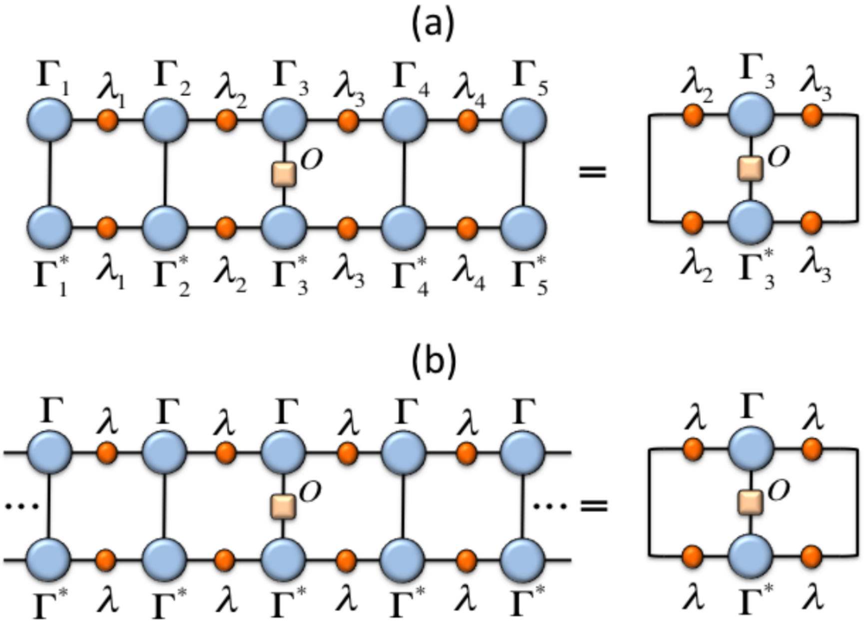

Figure 4.4: Examples of calculation of the expectation value of a single-site observable for an MPS in canonical form. Panel (a): finite MPS with 5 sites and operator acting on site 3. Panel (b): infinite MPS with single-site unit cell. Taken from [93].

in Fig. 4.3. The canonical form of MPS has some convenient properties that justify its use. First of all, it simplifies the calculation of expectation values of local operators, as can be seen in Fig. 4.4. Indeed, quantum mechanical operators, for instance the model Hamiltionan, can be written in the formalism of Matrix Product Operators (MPO) [92] and the diagrammatic representation can be exploited again: only the tensors and the eigenvalues related to the site on which the operator acts are relevant, while all the others are wiped out thanks to the normalization condition intrinsic to the canonical form.

In addition to that, this form provides a recipe for the decimation step in numerical simulations: we just keep the largest D Schimdt coefficients at every bond and this is optimal for finite systems as long as truncation is local, such that it implies only a modification of the tensors involved in the truncated index.

Chapter 5

Frustrated extended Bose-Hubbard model

Previous studies on the frustrated Bose-Hubbard model highlighted the presence of a chiral superfluid phase, both at half filling [110, 111] and at unit filling [112]. On top of that, theoretical works on the extended Bose-Hubbard model found proof of the existence of supersolidity at non-commensurate filling [113, 71].
We aim at detecting a novel chiral supersolid phase in the phase diagram of the frustrated extended Bose-Hubbard model (FEBHM) at commensurate filling, thus showing that frustration is a new physical mechanism that allows to obtain supersolidity and even a new kind of supersolid.
Here, we start from some preliminary results that serve as the basis for the project, then we introduce the model under study and we propose an experimental setup for its realization. Finally, we highlight the main difficulties we met in our computational analysis.

Let us start by considering an XXZ chain of spins-1/2 with both nearest and next-nearest neighbor interaction, denoted as J_1 and J_2 respectively, which is described by the following Hamiltonian:

$$H = \sum_{n=1}^{2} \sum_{i} J_n \left(S_i^x S_{i+n}^x + S_i^y S_{i+n}^y + \Delta S_i^z S_{i+n}^z \right) \ , \tag{5.1}$$

where we have introduced the components of the spin operator $\mathbf{S}_i$ at a site i and Δ encodes the anisotropy along the z-component. It has been shown that such a model exhibits frustration as long as the interaction between next-nearest neighbors is antiferromagnetic, that is $J_2 > 0$, independently of the nature of the nearest neighbor interaction J_1 [76]. In particular, in the case of $J_1 < 0$ and $J_2 > 0$ [79], the ground-state phase diagram displays a region where the system has a gapless phase with chiral vector order and this is true also for the case $\Delta = 0$, when the model reduces to the triangular spin-1/2 XY model. Notice that the latter can be seen as a triangular lattice with plaquettes as in Fig. 3.4, with nearest neighbor couplings on diagonal links and next-nearest neighbor coupling on the horizontal one. Therefore, it is evident that frustration is introduced in the model whenever only one or all three links are antiferromagnetic.

Interestingly, we can exploit the mapping $S_j^x = \frac{1}{2}\left(b_j^\dagger + b_j\right)$, $S_j^y = \frac{1}{2i}\left(b_j^\dagger - b_j\right)$ for $\Delta = 0$, in order to rewrite (5.1) into a frustrated Bose-Hubbard model at density 1/2 in the strong coupling limit, whose Hamiltonian is written as:

$$H = -\sum_i \left[t_2\left(b_i^\dagger b_{i+2} + h.c.\right) + t_1\left(b_i^\dagger b_{i+1} + h.c.\right)\right] + \frac{U}{2}\sum_i n_i\left(n_i - 1\right) \quad , \tag{5.2}$$

where $b_i^\dagger$ and b_i are the bosonic creation and annihilation operators, whereas $n_i = b_i^\dagger b_i$ is the number operator. The coefficients t_1 and t_2 are the amplitudes of nearest and next-nearest neighbor hopping respectively, while U is the interaction between bosons sharing the same site. The system can be seen as a triangular ladder with nearest neighbor processes on diagonal links and next-nearest neighbor processes on horizontal ones, see Fig. 5.1(c).

Indeed, the model (5.2) has been shown to exhibit a chiral superfluid phase when frustration is introduced by a suitable choice of the signs of t_1 and t_2 [111], which act analogously as the coefficients J_1 and J_2 of the spin model. In the reference, for reasons of experimental feasibility that will be discussed later, they chose $t_2 > 0$ and staggered nearest neighbor hopping, with t_1 being alternatively positive and negative, leading to:

$$H = -\sum_i \left[t_2\left(b_i^\dagger b_{i+2} + h.c.\right) + t_1\left(-1\right)^i\left(b_i^\dagger b_{i+1} + h.c.\right)\right] + \frac{U}{2}\sum_i n_i\left(n_i - 1\right) \quad . \tag{5.3}$$

We are interested in the effect of longer-range interaction on such a model, therefore we want to study a richer Hamiltonian:

$$\begin{aligned} H = &-\sum_i \left[t_2\left(b_i^\dagger b_{i+2} + h.c.\right) + t_1\left(-1\right)^i\left(b_i^\dagger b_{i+1} + h.c.\right)\right] \\ &+ \frac{U}{2}\sum_i n_i\left(n_i - 1\right) + V\sum_r \frac{1}{r^3}\sum_i n_i n_{i+r} \quad , \end{aligned} \tag{5.4}$$

where the last term has the aim of encoding dipolar interactions, which are known to decay with distance as r^{-3} between two particles at sites i and j with $r = |i - j|$. In order to include this type of interaction in experiments, the use of atoms with a strong magnetic moment is required. We have verified that the inclusion of interactions beyond next-nearest neighbors does not influence the results, therefore in the simulations we truncate the term at $r = 2$.

We want to study the system at unit filling $\bar{n} = \frac{\#\, bosons}{\#\, sites} = 1$ and we set the energy scale in Equation (5.4) by fixing $t_1 = 1$, so that all energy quantities are expressed in units of t_1.

The element that introduces geometric frustration is the staggering in the next-nearest neighbor hopping term. Notice that this Hamiltionan is invariant under gauge transformations that conserves the π-flux in a loop around a triangular plaquette of the lattice: for the Hamiltonian (5.4), if $t_2 > 0$, a particle completing a loop encounters two positive hopping amplitudes and a negative one on a diagonal link, which is equivalent to gaining a phase factor π. But this choice is not unique and, after checking the equivalence of the results, for simplicity in performing our simulations we actually remove the staggering on the sign of the nearest neighbor hopping amplitude and we always take negative next-nearest neighbor hopping amplitude $t_2 < 0$.

In [111], an experimental setup for the realization of such a model by using Cesium atoms is discussed. We want to propose a similar implementation, where Cesium is instead replaced by Dysprosium: atoms of this type are characterized by a strong magnetic moment and exhibit long-range dipolar interactions [47]. The idea is to take a two-component Bose gas trapped in a 1D state-dependent optical lattice with L sites, as shown in Fig. 5.1. The two atomic species, which are two different energy states of Dysprosium atoms, denoted as $|l\rangle$ (lower energy state) and $|h\rangle$ (higher energy state), are disposed to form a state-dependent optical lattice at the anti-magic wavelength λ. This can be seen as two superimposed sublattices displaced by a length $\lambda/4$, so that the minima of a sublattice correspond to the maxima of the other one. The intra-species hopping amplitudes are the same for the two sublattices, $t_l = t_h = t_2$, and they can be seen as the amplitude of next-nearest neighbor hopping in the full lattice. On the other hand, the intra-species interactions U_{ll} and U_{hh} and the inter-species one U_{lh} may be different. Adjacent sites belonging to different sublattices are connected by Raman-assisted tunneling processes (green arrows in Fig. 5.1), encoded as $t_{eff}e^{i\theta j}$ with i the imaginary unit and j the lattice site index. Thus, the full system is described by the following Hamiltonian:

$$\begin{aligned} H = &- \sum_j \left[t_2 \left(b_j^\dagger b_{j+2} + h.c. \right) + t_{eff} e^{i\theta j} \left(b_j^\dagger b_{j+1} + h.c. \right) \right] \\ &+ \sum_j \left[\frac{U_{ll}}{2} n_{2j-1} \left(n_{2j-1} - 1 \right) + \frac{U_{hh}}{2} n_{2j} \left(n_{2j} - 1 \right) \right] \\ &+ U_{lh} \sum_r \frac{1}{r^3} \sum_j n_j n_{j+r} \quad . \end{aligned} \tag{5.5}$$

As we explained before, we truncate the extent of the dipolar interaction at next-nearest neighbor sites. We now perform a specific choice of parameters

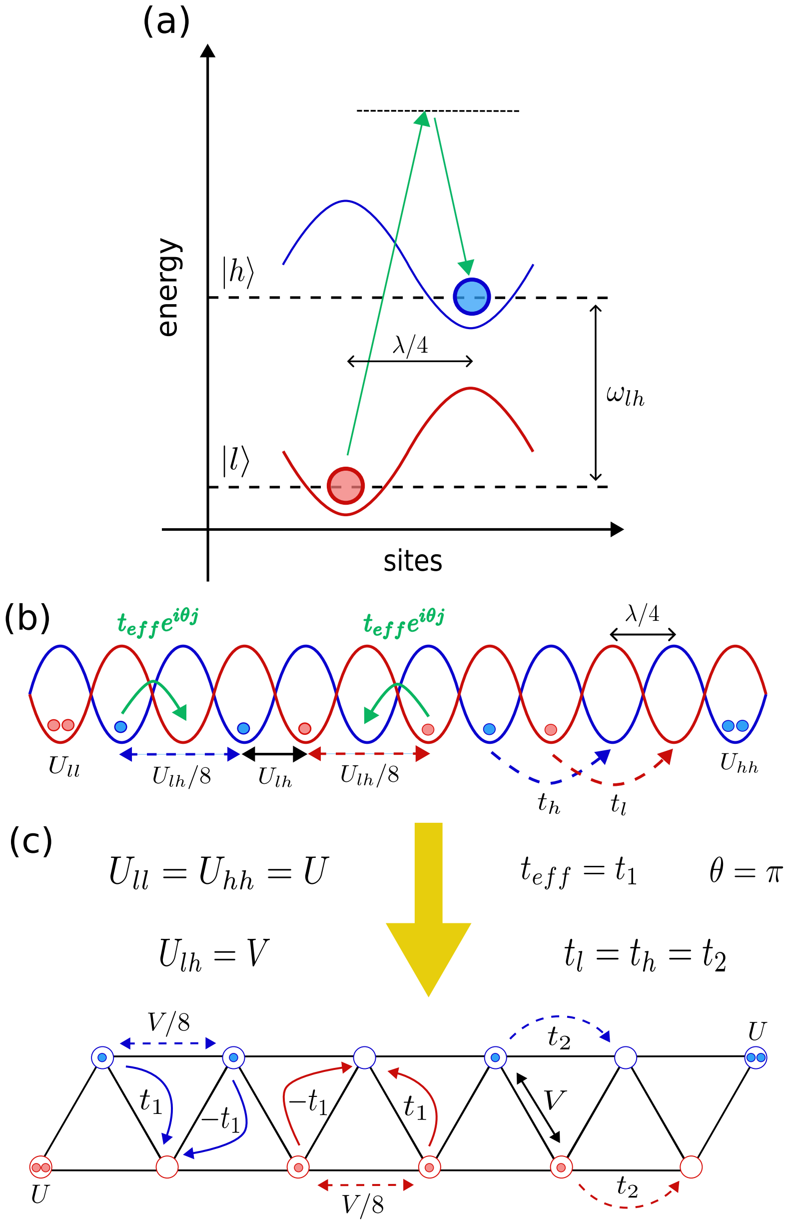

Figure 5.1: Schematics of the experimental setup to realize Equation (5.4). Top panel: state-dependent optical lattice at the anti-magic wavelength λ, with Raman-assisted tunneling (green arrows) between nearest neighbor sites separated by energy difference ω_{lh}. Middle panel: shifted sublattices with effective spacing $\lambda/4$ described by Equation (5.5), all interactions and hopping processes are displayed. Bottom panel: specific choice of parameters that yields model (5.4) on a triangular lattice.

that allows us to obtain our model (5.4), as shown in Fig. 5.1(c). In particular, we take intra-species interactions to be equal $U_{ll} = U_{hh} = U$ and we set the inter-species one $U_{lh} = V$. Then, we fix $t_{eff} = t_1$ with $\theta = \pi$, while we had already assumed $t_l = t_h = t_2$. This finally yields a triangular lattice with nearest neighbor processes, including staggered hopping, along diagonal links and next-nearest neighbor processes, with correctly reduced density-density interaction, along horizontal ones.

Computational aspects

As we stated before, we have the goal of detecting a chiral supersolid phase, emerging from a combination of geometric frustration and beyond-onsite interactions. As mentioned in Chapter 2, up to now the studies on supersolidity have been mainly limited to mean-field regimes, where the effect of quantum fluctuations is negligible. For this reason, observing a supersolid phase in a deeply quantum regime would be quite innovative, therefore that is the setting that we want to consider. However, this means taking into account quantum fluctuations, represented in the model Hamiltonian by the hopping terms, but this cannot be achieved through analytical approaches.

We must then resort to quasi-exact simulation methods: we use DMRG to study the model (5.4), exploiting both the finite and the infinite version of this algorithm. In particular, we make use of a free-access Python package called TeNPy [114], which is based on the formulation of DMRG in terms of MPS.

In addition to the deeply quantum regime, another element of complexity is introduced by frustration. Indeed, when the amplitude of next-nearest neighbor hopping is large, the system is frustrated and chiral phases might emerge. In such a condition, the quantum entanglement between particles becomes very large and this implies that a bigger portion of the Hilbert space must be considered in order to correctly capture the physics of the ground-state. Therefore, we need to introduce an higher cut-off in the truncation step of DMRG, keeping a large amount of singular values of the reduced density matrix, as its eigenvalue spectrum does not decay fast.

More precisely, for building the phase diagrams that are going to be shown in Chapter 6, we use iDMRG with unit cell of length 6 and we consider a ramp for the bond dimension (BD) starting from $BD = 300$ and increasing by 100 every 20 sweeps up to $BD = 800$, with a maximum number of sweeps equal to 250. This gradual increase in the bond dimension allows to initially suppress quantum superpositions between different states, due to the limited size of the Hilbert space considered, and to later reduce the truncation error by taking into account a large number of eigenvalues of the reduced density matrix. More information about the computational procedure is given at the beginning of the following chapter.

An example of an input script is shown in Appendix A and all the details of the simulations can be found there.

Chapter 6

Results

We are interested in building the phase diagram of the model (5.4) in the two following cases:

- fixed onsite interaction U;
- fixed next-nearest neighbor hopping amplitude t_2.

In this chapter, we explore this two situations and we take a detailed look at the different phases detected and their properties.
Before moving on, let us remark that all the results are obtained for unit filling, that is $\bar{n} = 1$, and with $t_1 = 1$, so that all energy quantities are expressed in units of t_1.

6.1 Ground-state phase diagrams

Before we show the actual results, some technicalities of the simulations must be addressed. First of all, we started working with the finite version of DMRG and an even number of sites, but this is problematic in the case of phases with a density wave profile, because of the degeneracy between the structures $2-0-2-0-...$ and $0-2-0-2-....$
As a matter of fact, since we consider open boundary conditions (OBC) the ground-state will have an higher occupation on the two extremal sites and a defect will form in the middle of the chain, as can be seen in Fig. 6.1. Note that this is not a computational artifact but a physical consequence of using OBC: it is convenient that both extremal sites are occupied, since they account for density-density interaction only from one neighbor, and this is possible with even sites only if the periodicity is inverted at some point along the chain.

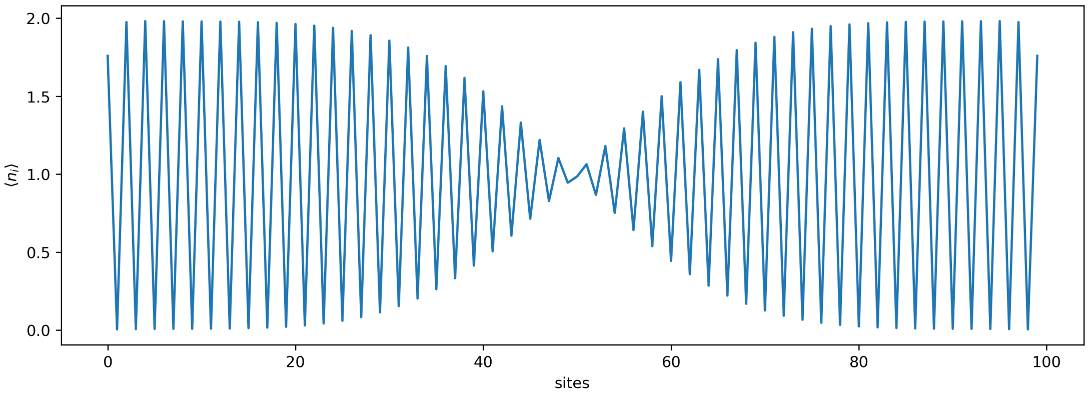

Figure 6.1: Example of the density profile $\langle n_i \rangle$ of a CDW-like phase for a finite chain with 100 sites. Both extremal sites are occupied and the difference in occupation between two neighbors reduces until the periodicity is inverted with the defect in the middle of the chain.

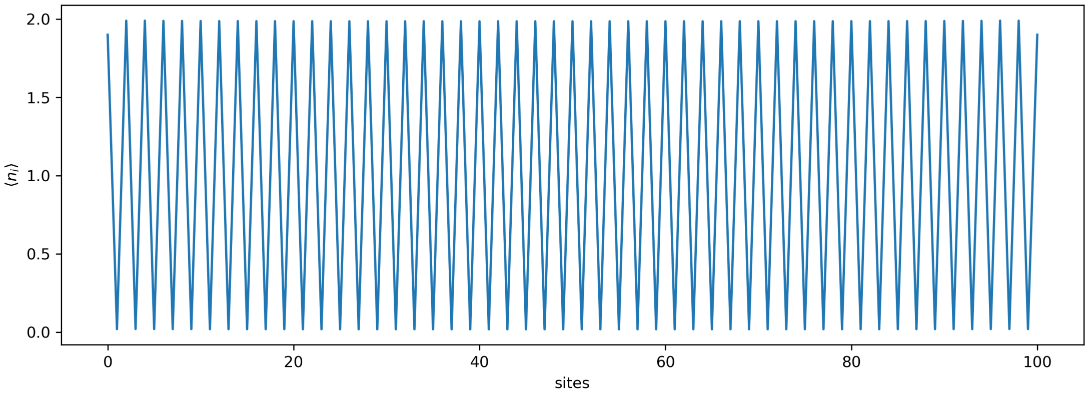

Figure 6.2: Example of the density profile $\langle n_i \rangle$ of a CDW-like phase for a finite chain with 101 sites. In this case, no defect is present thanks to the choice of an odd number of sites.

Therefore, we moved to an odd number of sites L, which allows to avoid this problem, and we considered a number of particles $N = L + 1$: this is aimed at lifting the intrinsic degeneracy present at exactly commensurate fillings, where either even or odd sites could be occupied. An example of the density profile in the case of a CDW is shown in Fig. 6.2 .
However, the use of finite size DMRG implies the necessity of a scaling analysis to extract reliable results, by considering systems of different sizes. For this reason, we finally chose to exploit iDMRG whenever is possible, in particular for building the phase diagrams, since this method approximates well the system in

the thermodynamic limit by construction.
Nonetheless, the infinite version of the algorithm cannot be used for the calculation of the so-called charge gap and, for that purpose, we were forced to go back to finite-size DMRG. Later on, we will illustrate how to correctly set up the simulations in such a case, as some expedients are required in order to avoid the problems mentioned above.

6.1.1 Phase diagram at fixed on-site interaction

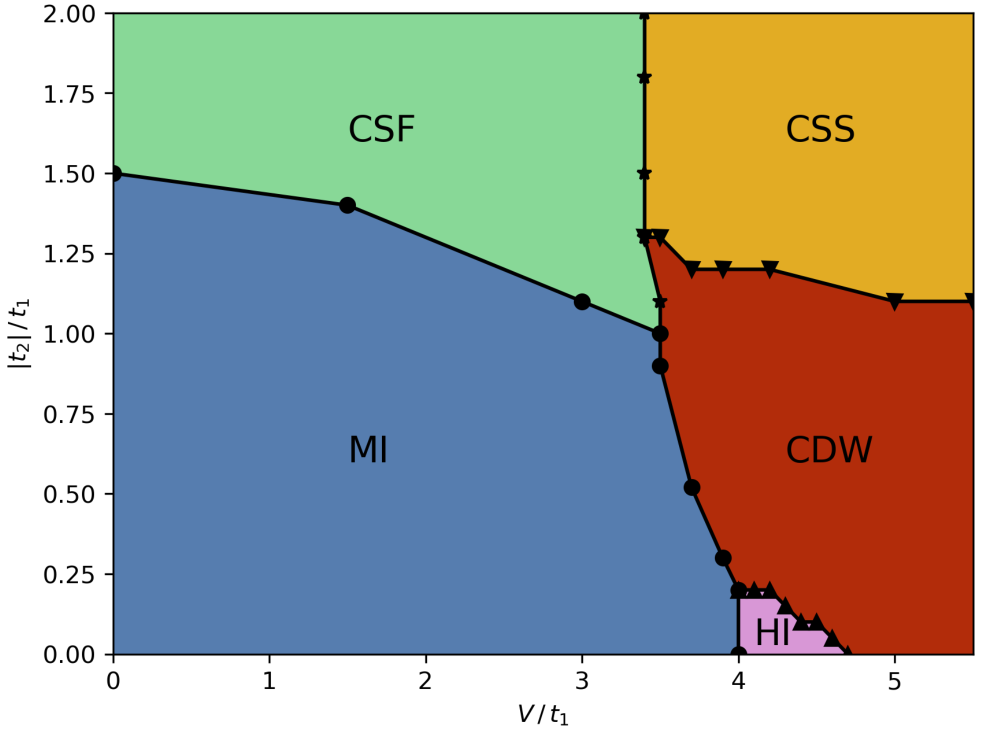

Figure 6.3: Phase diagram of the 1D FEBHM at $U = 6$ in the $V - t_2$ plane. From the bottom, the blue region corresponds to a Mott insulator (MI), the violet one to an Haldane insulator (HI) and the red one to a charge density wave (CDW). At the top, the green color signals a chiral superfluid (CSF) and the orange color a chiral supersolid (CSS).

The phase diagram at fixed onsite interaction $U = 6$ is shown in Fig. 6.3, where the nearest-neighbor interaction V varies on the x-axis, while on the y-axis we consider the absolute value of the next-nearest neighbor tunneling t_2.
For low values of both the parameters the system is a Mott insulator (MI), characterized by the absence of phase coherence, that is it exhibits an exponential decay

with distance of the so-called superfluid correlator:

$$g_1\left(|i-j|\right) = \langle b_i^\dagger b_j \rangle \ , \tag{6.1}$$

and a finite value of the parity operator:

$$P\left(j\right) = e^{i\pi \sum_{k<j} \delta n_k} \ , \tag{6.2}$$

where we have introduced $\delta n_k = n_k - \bar{n}$. When V is increased, for values of $|t_2|$ close to zero, there is a small region where the system behaves as an Haldane insulator (HI), which is a simmetry protected topological (SPT) phase with hidden order, signaled by a finite value of the z-string operator at long distances:

$$O_z\left(|i-j|\right) = \delta n_i e^{i\pi \sum_{i<k<j} \delta n_k} \delta n_j \ . \tag{6.3}$$

By further increasing V or by considering higher values for $|t_2|$, we encounter a charge density wave (CDW), that is an insulating phase characterized by a periodic modulation in the density profile. This is signaled by a finite value of the local order parameter:

$$\delta N = \frac{1}{L} \sum_i \left(-1\right)^i \delta n_i \ , \tag{6.4}$$

which implies the presence of a peak, located at $k = \pi$ for unit filling, in the structure factor:

$$S\left(k\right) = \frac{1}{L} \sum_r \langle n_0 n_r \rangle e^{-ikr} \ , \tag{6.5}$$

namely the Fourier transform of the density-density correlator $\langle n_i n_j \rangle$.
However, these three phases are not particularly interesting: as a matter of fact, they can be observed in the phase diagram of a simple one-dimensional EBHM at unit filling for such an high value of the onsite interaction U, as shown in Fig. 3.3.

More exciting physics emerges when the next-nearest neighbor hopping amplitude becomes comparable and even larger with respect to the nearest neighbor one: indeed, in this case the system is really frustrated and chiral order is observed. In the case of bosons, we define the following chiral correlator:

$$k^2\left(|i-j|\right) = \langle k_i k_j \rangle \tag{6.6}$$

with

$$k_j = -\frac{i}{2}\left(b_j^\dagger b_{j+1} - b_{j+1}^\dagger b_j\right) \ ,$$

which is nothing but a current operator. Indeed, k_j contains the difference between hopping from site $j+1$ to j and from site j to $j+1$. Thus, this equals to measuring

the preference of particles for moving left or right. When the time-reversal symmetry is broken and currents are present, the expectation value (6.6) will be finite even for very long distances $|i-j|$.
Going back to our phase diagram, for low values of V, more precisely when the onsite interaction dominates over the repulsion between neighboring particles, we find a chiral superfluid (CSF). This phase is characterized by a power-law decay of the superfluid correlator $g_1\left(|i-j|\right)$ (6.1), together with a finite value of the chiral correlator $k^2\left(|i-j|\right)$ (6.6), signaling the presence of finite currents between nearest neighbor sites. In addition, we also find a double-peaked profile of the momentum distribution defined as the Fourier transform of g_1, namely:

$$N\left(k\right)=\frac{1}{L}\sum_{r}g_1\left(r\right)e^{-ikr}\ , \tag{6.7}$$

see Fig. 6.5(c) as an example, which implies the spontaneous breaking of the time-reversal simmetry as we will explain in the following.
Finally, when V is increased and it dominates over U, it is convenient for the system to acquire a density wave profile, but still keeping phase coherence along the chain. This means that we have the combination of diagonal long-range order (DLRO), in the form of a periodic modulation of the density profile, and off-diagonal long-range order (ODLRO), signaling the presence of a partial frictionless flow of particles, typical of superfluids: this is exactly the condition for identifying a supersolid. On top of that, this phase exhibits also the features of a chiral phase, with a non-zero value of the chiral correlator at long distances and two pronounced peaks in the momentum distribution, as can be seen again in Fig. 6.5(c). We thus recognize this phase as a chiral supersolid (CSS) with lattice periodicity, which constitutes the most relevant result of this project.
We will further elaborate on these chiral phases in the next section of this chapter.

Let us mention the fact that one could expect to observe a thin region with a chiral Mott insulating phase between the MI and the CSF, as is the case in [112]. However, by analyzing our results we are not able to determine whether there really is a different phase in between the two we identified or we just witness an extremely slow transition. Since we are inclined to believe the second option is correct, we decide to exclude this possible additional phase from our analysis.

6.1.2 Phase diagram at fixed next-nearest neighbor hopping amplitude

In the case of fixed next-nearest neighbor hopping amplitude $|t_2|=1.3$, we vary V along the x-axis, while U is scanned along the y-axis. For our choice of values, due to the moderately high absolute value of t_2 needed to see the effect of frustration

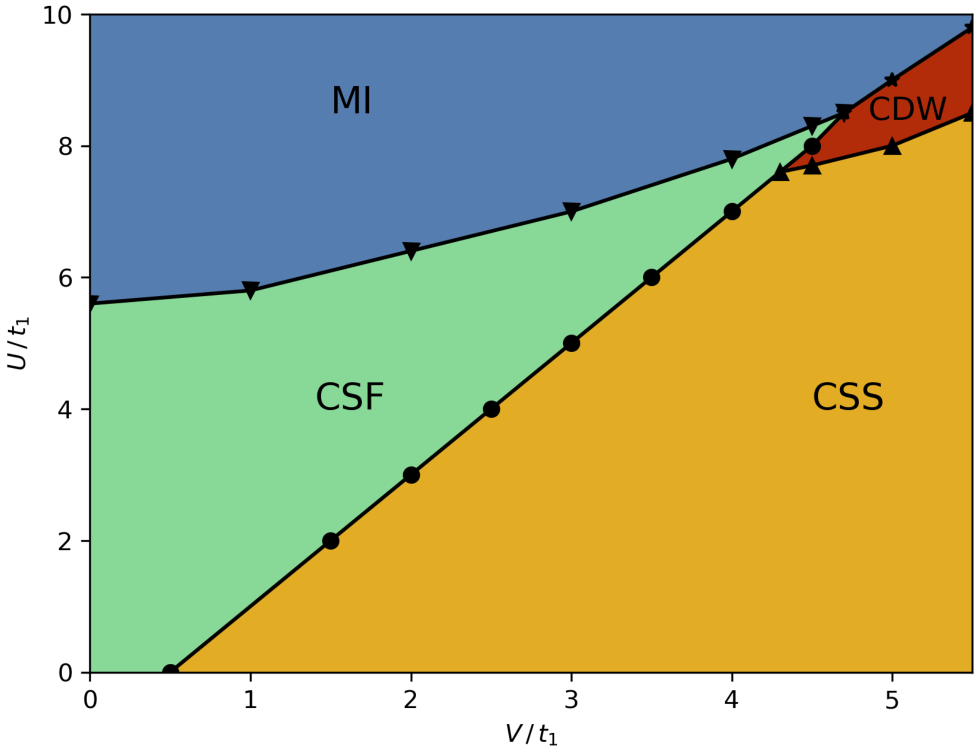

Figure 6.4: Phase diagram of the 1D FEBHM at $|t_2| = 1.3$ in the $V - U$ plane. The color code and the acronyms are the same as Fig. 6.3.

and the emergence of chirality, no Haldane insulating phase appears.
Similarly to the previous case, for low values of U, when the repulsion between neighbors dominates over the onsite interaction, we find a chiral supersolid. In the opposite situation, namely for predominant onsite interaction, the system is instead in a chiral superfluid phase. Finally, by increasing U the system becomes frozen in a MI phase for low values of V or in a CDW phase when the repulsion between neighbors is strong enough.

6.2 Characterization of the chiral phases

In this section, we want to focus on the two most interesting states of matter we found in the phase diagrams of our model, namely the chiral superfluid and the chiral supersolid, considering the main features that characterize them. In Fig. 6.5 we show some relevant quantities for two exemplary CSF and CSS.
Let us start from Fig. 6.5(a), where the density profile $\langle n_i \rangle$ is reported for a segment of length 200 sites of an infinite MPS. We see that, while in the superfluid the

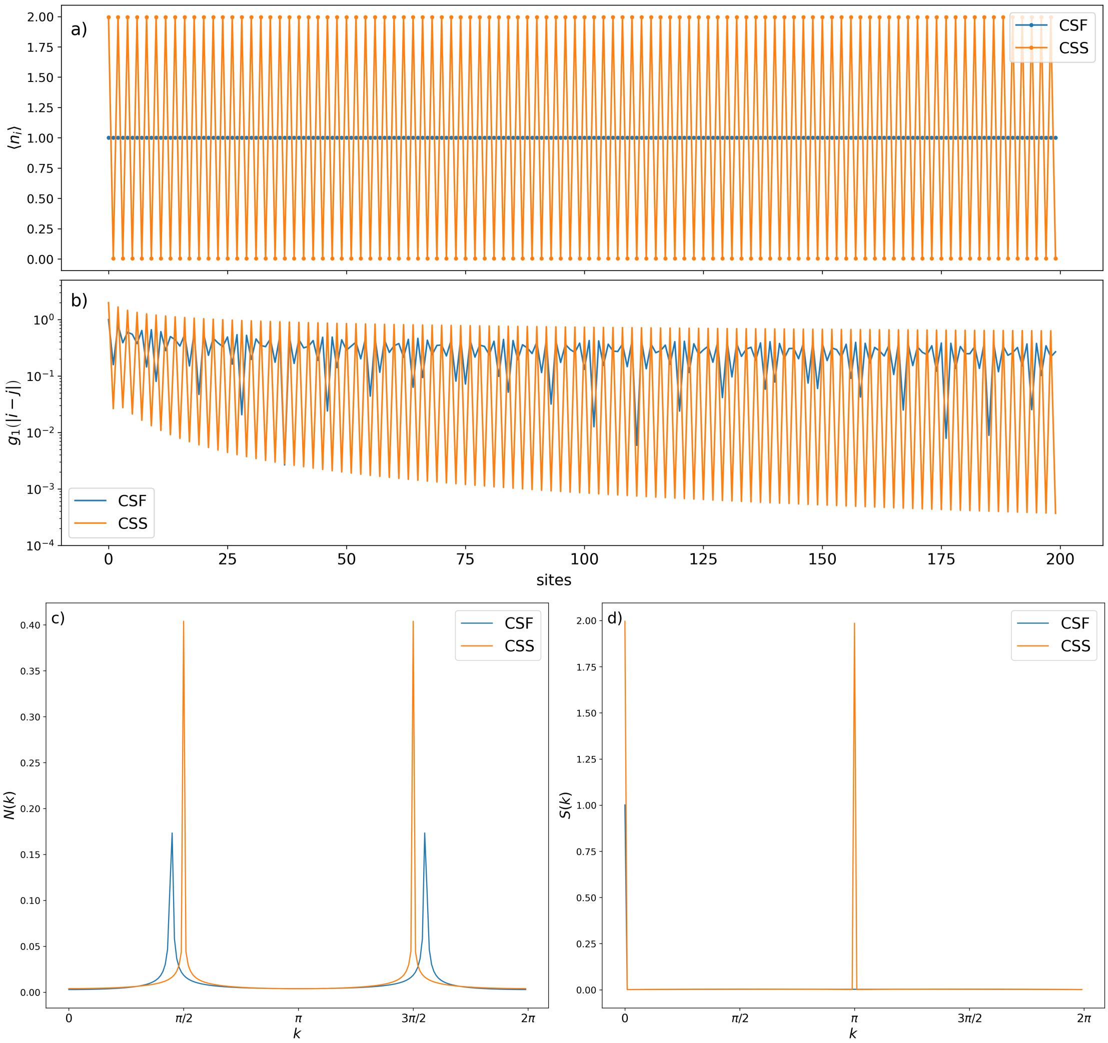

Figure 6.5: Examples of the chiral superfluid (CSF, blue) and the chiral supersolid (CSS, orange) phases taken for $U = 6$, $|t_2| = 1.6$ and $V = \{3.0,\ 4.5\}$. Two upper panels: **a)** local density and **b)** superfluid correlator for the two phases computed over a segment of length 200 sites of an infinite MPS. Two bottom panels: **c)** momentum distribution (6.7) and **d)** structure factor (6.5).

occupation of each site averages 1, the supersolid exhibits a periodic modulation that gives it an almost perfect $\ldots - 2 - 0 - 2 - 0 - \ldots$ repeated profile. This structure has the same periodicity as the lattice, for this reason we talk about a lattice supersolid.

In Fig. 6.5(b), we display the behaviour of the superfluid correlator (6.1) for the two phases, again for a segment of 200 sites. In both cases, the decay is extremely slow and it allows us to claim the presence of ODLRO along the chain. Nevertheless, we notice strong modulations, especially in the CSS, signaling lower coherence between nearest neighbor sites and very high coherence between next-nearest neighbor ones.

In the lower panels instead, we move our analysis to the momentum space. In particular, we have the momentum distribution (6.7) in Fig. 6.5(c) and the structure factor (6.5) in Fig. 6.5(d). The latter exhibits a peak at $k = \pi$ in the case of the supersolid, confirming the spontaneous breaking of the translational symmetry that implies the presence of DLRO in the system, while no peak is observed for the superfluid, except for the one at $k = 0$, which does not signal any periodicity.

The momentum distribution instead is extremely interesting: in both the phases, two peaks at $k \neq 0$ are present. More precisely, these peaks are exactly at $k = \{\pi/2\,, 3\pi/2\}$ in the CSS and quite close to these values in the CSF. Due to this feature, we can say that these two phases are actually chiral. Indeed, in a simple superfluid (or supersolid) one would observe only a peak at zero momentum, implying the presence of a single minima in the dispersion relation of the model at $k = 0$. Therefore in that case, the time-reversal symmetry is not broken. Instead in our situation, two symmetric peaks in $N(k)$ corresponds to two symmetric minima in the dispersion relation, signaling the spontaneous breaking of the time-reversal symmetry and, as consequence, the presence of finite currents between sites.

6.3 Order parameters along cuts of phase diagrams

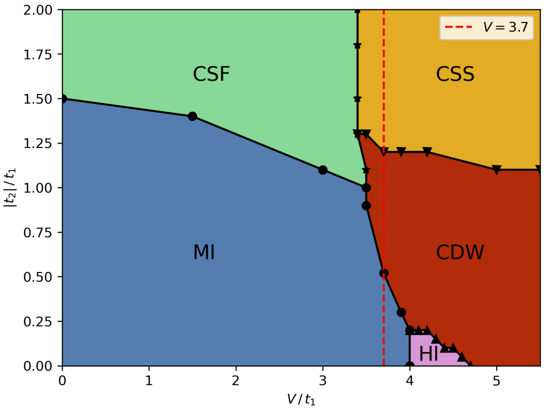

Figure 6.6: Vertical cut at $V = 3.7$ in the phase diagram of Fig. 6.3.

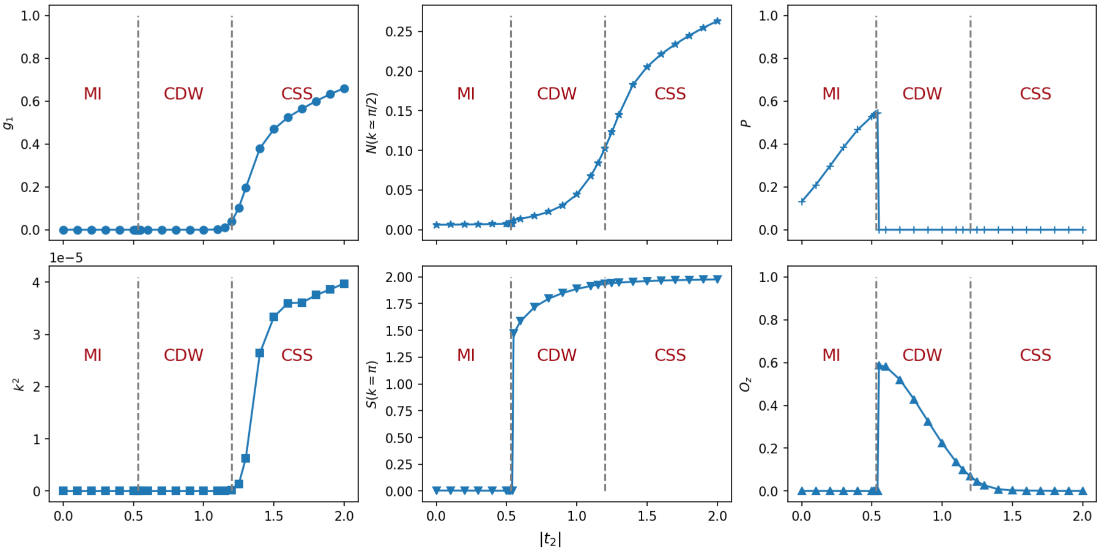

Figure 6.7: Order parameters for different values of $|t_2|$ and fixed $U = 6$, $V = 3.7$. Top: superfluid correlator, momentum distribution around $\pi/2$, parity. Bottom: chiral correlator, structure factor at π, string. Superfluid correlator, chiral correlator, parity and string are computed at a distance of 200 sites.

In order to give a more detailed picture, we study now a vertical cut in both the phase diagrams shown before by looking at all the significant correlators and order parameters.

First of all, let us consider the phase diagram at fixed onsite interaction $U = 6$ (Fig. 6.3): we set $V = 3.7$, see Fig. 6.6, and vary the values of the next-nearest neighbor hopping amplitude $|t_2| \in [0.0, 2.0]$, as shown in Fig. 6.7.
Starting from low values of t_2, the system is a Mott insulator. Indeed, the superfluid correlator $g_1\left(|i-j|\right)$ (6.1) decays exponentially and is identically zero at long distance and the same can be said for the chiral correlator $k^2\left(|i-j|\right)$ (6.6). In this phase, no symmetry is broken: as a consequence, no peak can be seen both in the momentum distribution $N\left(k\right)$ (6.7) and in the structure factor $S\left(k\right)$ (6.5). Instead, we notice a finite values for the parity operator P (6.2), while the string O_z (6.3) is clearly zero here, so everything is consistent with a MI.
Around $|t_2| = 0.52$, the system undergoes a sharp transition to a charge density wave, again characterized by exponentially decaying superfluid and chiral correlators. However, in this case we can see a peak at π in the structure factor, whereas the situation of parity and string operators is reversed with respect to the previous case, being P vanishing and O_z finite.
Finally, we observe a very slow transition from a charge density wave to a chiral

supersolid. Here $g_1(|i-j|)$ decays with a power-law, being finite even at long distance, and $k^2(|i-j|)$ exhibits higher values, in agreement with the presence of peaks at $\pi/2$ and $3\pi/2$ in the momentum distribution. The periodic modulation of the CDW is kept, as signaled by the structure factor, while both parity and string are zero.

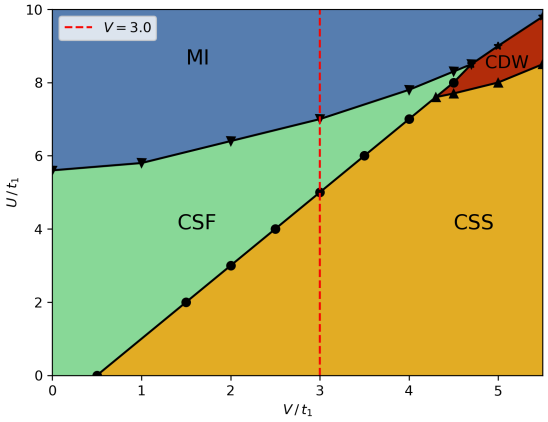

Figure 6.8: Vertical cut at $V = 3.0$ in the phase diagram of Fig. 6.4.

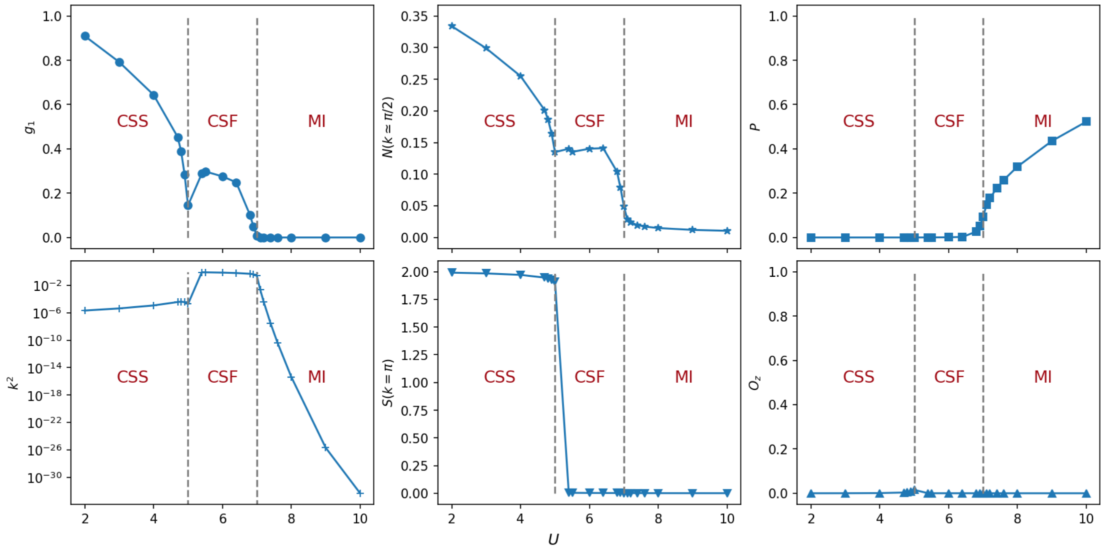

Figure 6.9: Order parameters for different values of U and fixed $|t_2| = 1.3$, $V = 3.0$. Top: superfluid correlator, momentum distribution around $\pi/2$, parity. Bottom: chiral correlator, structure factor at π, string. Superfluid correlator, chiral correlator, parity and string are computed at a distance of 200 sites.

We perform the same analysis in the case of the second phase diagram, where we have fixed the next-nearest neighbor hopping $|t_2| = 1.3$ (Fig. 6.4). In this case, we consider a vertical cut for $V = 3.0$, see Fig. 6.8, and we look at the quantities of interest for onsite interaction $U \in [2, 10]$.
Starting from low values of U, we find a CSS with all its characteristic features, until a sharp phase transition to a CSF occurs at $U = 5$. Here we have high values of superfluid and chiral correlators at long distance, with two symmetric peaks in the momentum distribution. The expectation value of both parity and string operators are identically zero and no peak is observed in the structure factor.
Finally, the systems undergoes a very slow transition to a MI, characterized by an exponential decay of both $g_1\left(|i-j|\right)$ and $k^2\left(|i-j|\right)$, while no peak is present in the momentum distribution and in the structure factor. Instead we notice an arising value of the parity, while the string stays at zero.

6.4 Charge gap

As mentioned before, iDMRG cannot be exploited when one wants to compute the charge gap (3.5), that was defined in Chapter 3. This quantity is related to an energy penalty that may be paid when a particle is added to or removed from the system. However, with the infinite version of the algorithm, we just define the unit cell and we lack full control over the exact number of particles in the chain. Therefore, we need to use finite-size DMRG and perform 3 different simulations for each fixed configuration of the parameters: one by giving as input an initial state at exact unit filling and two initializing the system away from unit filling by removing and adding a particle, respectively.
This requires for some technicalities in the simulations, in particular in the regions of the phase diagrams where we find phases with a periodic modulation, namely CDW and CSS. First of all, we choose an even number of sites and this forces us to remove the central defect mentioned in Section 6.1. In order to do that and avoid the consequent emergence of a double degeneracy in the ground-state, we fix the number of particles at the boundaries of the finite chain by means of high absolute values of the chemical potential at those two sites. More precisely, it is sufficient to modify the model (5.4) by adding a local term either at first or last site that disfavors the occupation of that site; in our case, we insert the term $100n_0$, acting on the first site since we label sites starting from 0.
Furthermore, the finite version of DMRG might produce results affected by finite-size effects and this can be avoided only by simulating very large systems. However, this would be extremely costly from the computational point of view; it is then convenient to perform a scaling towards the thermodynamic limit by running simulations for systems of different sizes and extracting the actual results from a

fitting of the output data.

Moving on to the expected results, in insulating phases (MI, HI, CDW in our case) the charge gap must be finite and they are said to be “gapped phases”. The reason is that, since these states are insulators, particles are fixed and the additional hole or particle either breaks the configuration, triggering a phase transition, or all the other particles have to be redistributed in order to keep the previous structure. For instance, in the case of a Mott insulator at unit filling, an added particle will move on top of the singly occupied sites.
On the other hand, in superfluids and supersolids the charge gap is expected to be zero and these phases are defined as “gapless”. In this case, an additional particle does not change the state of the system and instead just blends together with the pre-existing sea of coherently moving particles. This is what we should observe in our CSF and CSS phases.

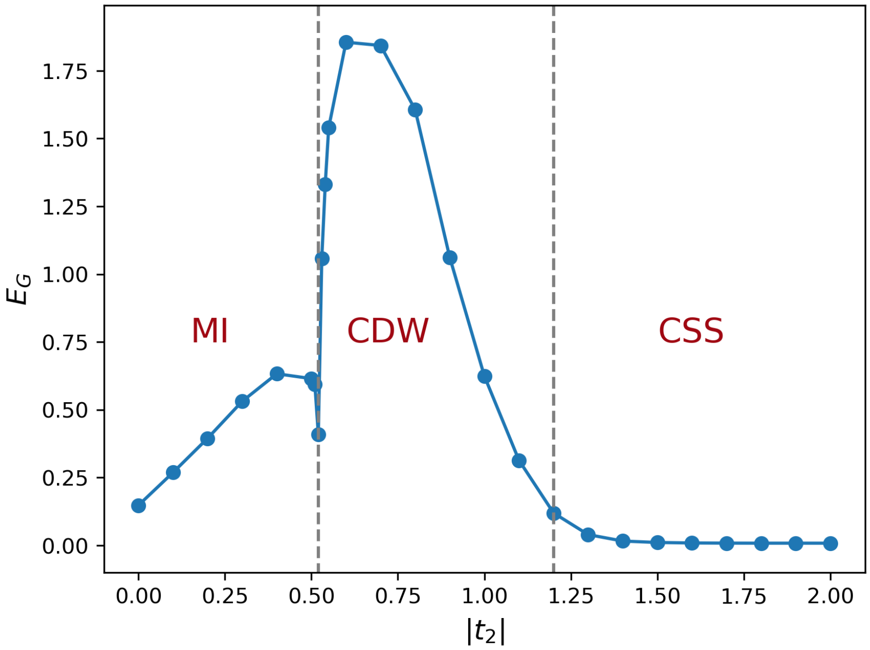

Figure 6.10: Value of the charge gap (3.5) for $|t_2| \in [0.0, 2.0]$ at fixed $U = 6$ and $V = 3.7$. Results obtained via scaling of data for different sizes $L = \{80, 100, 120, 140, 160\}$ with a 4-th order polynomial, see Fig. 6.11.

In order to confirm the nature of the phases we detected, we consider the charge gap along the same vertical cut as in Fig. 6.6, 6.7, that is for fixed $U = 6$ and $V = 3.7$. The results are shown in Fig. 6.10 and are obtained from a scaling of the data from simulations of chains of length $L = \{80, 100, 120, 140, 160\}$. More precisely, we fitted the data as a function of $1/L$ to a polynomial function of the 4-th order, $f(x) = a\,x^4 + b\,x^3 + c\,x^2 + d\,x + e$, for all values of t_2 in the selected interval. The value of the function at $L \to \infty$, namely the parameter e, is then taken as the value of the charge gap in the thermodynamic limit. Examples of these fits for the three phases present along the considered cut are displayed in Fig. 6.11.

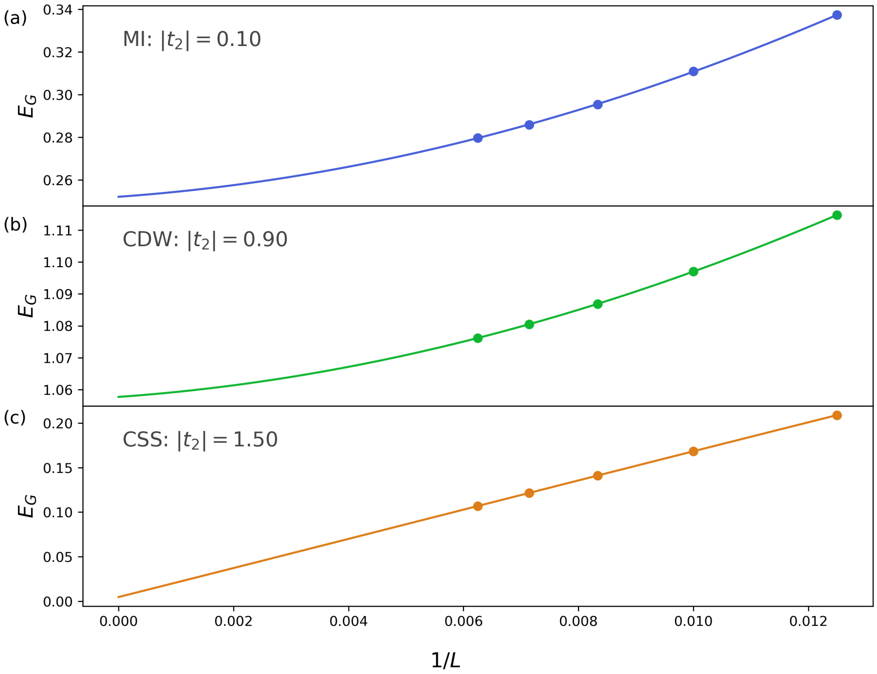

Figure 6.11: Examples of scaling analysis for the charge gap in the different phases. The solid lines represent the fitting functions, while the dots are the values of the gap at sizes $L = \{80, 100, 120, 140, 160\}$. Panel (a): Mott insulator at $|t_2| = 0.1$. Panel (b): charge density wave at $|t_2| = 0.9$. Panel (c): chiral supersolid at $|t_2| = 1.5$.

The results are in agreement with our expectations, as the charge gap is finite in the regions of MI and CDW, while it is zero for the CSS. Nevertheless, a couple of remarks are needed.

First of all, in the region of the Mott insulator the gap is quite small, especially for low values of $|t_2|$, see for instance Fig. 6.11(a). Actually, this is coherent with the fact that, for these points, the superfluid correlator g_1 decays exponentially but still quite slowly for a MI, due to the vicinity to a critical point and the limited accuracy of the simulations in such a situation. Therefore, the value of the charge gap is expected to be modest.

In the second place, we have a first-order transition between the MI and the CDW, which is quite abrupt, and the charge gap increases rapidly right after the transition value, located at $|t_2| \sim 0.52$. Instead, at the transition from charge density wave to chiral supersolid we observe a smooth decay towards zero of the value of the gap, which reflects the slow change of the order parameters in this case, as we have seen in Fig. 6.7. Notice that a similar behavior can be observed in the transition between the Mott insulator and the chiral superfluid: this leads use to recognize these transitions as being of the Berezinskii-Kosterlitz-Thouless type [67, 68].

Chapter 7

Outlook and conclusion

In this work, we first reviewed the theory behind supersolidity, which is an exotic phase of matter characterized by the coexistence of the properties of superfluids, featuring a frictionless flow of particles, and of solids, where a periodic modulation in the local density profile is observed.
Despite being theoretically predicted in 1950s, the existence of such quantum state has been elusive for many decades. After some unsuccessful attempts, the experimental realization of supersolidity was achieved unambiguously in quasi-1D geometries only in 2019, thanks to the developments in the experimental control of ultracold dipolar gases in optical lattices. These systems are formed by atoms with a strong magnetic moment, that causes the appearance of a long-range repulsive interaction, whose presence is fundamental for the emergence of supersolidity.
These experimental observations were obtained in regimes where quantum fluctuations are negligible, so that systems can be correctly described through mean-field approximations. Since we were interested in the study of systems in a deeply quantum regime, we needed to resort to numerical simulations. In particular, we exploited the Density Matrix Renormalization Group (DMRG) algorithm, which is the most powerful method for the identification of the ground-state phases of strongly correlated systems. Thus, we reviewed the basics of the algorithm and its useful reformulation in terms of Matrix Product States (MPS).

After that, we moved to the derivation of the well-known Bose-Hubbard model (BHM) in one dimension, which takes into account hopping processes between nearest neighbor lattice sites and onsite interactions between bosons. This model can be expanded by considering the interaction between nearest neighbor sites, thus obtaining the extended Bose-Hubbard model (EBHM).
Then, we studied a further enriched version of the EBHM by introducing geometrical frustration into the picture, through the addition of hopping processes between next-nearest neighbor sites. On top of that, we included also dipolar interactions

between particles. We were interested in studying the system at commensurate fillings and we chose to fix the average filling to 1.
The main goal of our work was to demonstrate that geometrical frustration can be used as a new physical mechanism to obtain supersolidity in a deeply quantum regime at integer filling. More precisely, we aimed at detecting a novel chiral lattice supersolid phase. In our case, chirality consists in a spontaneous breaking of the time-reversal symmetry, which in turn causes the presence of finite net current between sites.

Our simulations performed with the infinite version of DMRG allowed us to build a rich phase diagram for the FEBHM under study. The results highlighted the existence of three different insulating phases when frustration does not play an important role: in particular, a Mott insulator, an Haldane insulator and a charge density wave. Instead, when frustration is relevant, two phases with broken time-reversal symmetry were observed: an already known chiral superfluid and a novel chiral lattice supersolid.
The latter constitutes the main achievement of our project, as it marks the discovery of a new exotic phase of matter, while also confirming that frustration is a useful tool to induce supersolidity. Moreover, these results are relevant because we witnessed the existence of a supersolid phase at unit filling, without the need of moving away from commensurate fillings, and in a regime that takes into account the role of quantum fluctuations.
It is important to highlight that this is not limited to theoretical studies, as we also proposed an experimental setup based on the use of Dysprosium atoms, that allows for the actual observation of the novel supersolid that we detected. In this setup, hopping amplitudes and interaction coefficients can be suitably tuned in order to explore the ground-states phase diagram.

Appendix A

Example script for iDMRG with TeNPy

```
import numpy as np

import tenpy
from tenpy.algorithms import dmrg
from tenpy.models.hubbard import BoseHubbardChain
from tenpy.networks.mps import MPS
from tenpy.networks.terms import TermList

import yaml

import h5py
from tenpy.tools import hdf5_io

from tenpy.models.hubbard import BoseHubbardModel
class BoseHubbardChain_nnn_int(BoseHubbardModel):

    default_lattice = "Chain"
    force_default_lattice = True

    def init_terms(self, model_params):
        # 0) Read and set parameters.
        t1 = model_params.get('t1', 1.)
        t2 = model_params.get('t2', 1.)
        U = model_params.get('U', 0.)
        V1 = model_params.get('V1', 0.)
        V2 = model_params.get('V2', 0.)
        mu = model_params.get('mu', 0)
        for u in range(len(self.lat.unit_cell)):
```

```
            self.add_onsite(-mu - U / 2., u, 'N')
            self.add_onsite(U / 2., u, 'NN')
        for u1, u2, dx in self.lat.pairs['nearest_neighbors']:
            self.add_coupling(-t1, u1, 'Bd', u2, 'B', dx, plus_hc=True)
            self.add_coupling(V1, u1, 'N', u2, 'N', dx)
        for u1, u2, dx in self.lat.pairs['next_nearest_neighbors']:
            self.add_coupling(-t2, u1, 'Bd', u2, 'B', dx, plus_hc=True)
            self.add_coupling(V2, u1, 'N', u2, 'N', dx)

from tenpy.tools.params import asConfig
from tenpy.networks.mps import build_initial_state

L = 6
values = np.linspace(2.0,5.0,7)
print(values)
tval = [-0.9,-1.1]
print(tval)

for t2 in tval:
    for V in values:
        model_params = {
            't1': 1. , 't2': t2 , 'U': 6. , 'V1': V , 'V2': V/8. , 'mu': 0. ,
            'L': L ,
            'bc_MPS': 'infinite' ,
            'n_max': 4 ,
            'conserve': 'best' ,
            'filling': 1.0
        }

        M = BoseHubbardChain_nnn_int(model_params)

        if V < 4.0:
            p_state = [1]*M.lat.N_sites
        else:
            p_state = [2,0]*(M.lat.N_sites//2)

        psi = MPS.from_product_state(M.lat.mps_sites(), p_state, bc=M.lat.bc_MPS)

        dmrg_params = {
            'mixer': True,
            'mixer_params':{
                'amplitude': 1.e-6,
                'decay': 1.5,
                'disable_after': 5
                },
```

```
            'max_E_err': 1.e-9,
            'max_S_err': 1.e-5,
            'max_sweeps': 250,
            'min_sweeps': 120,
            'N_sweeps_check': 10,
            'chi_list':{
                0: 300,
                20: 400,
                40: 500,
                60: 600,
                80: 700,
                100: 800
            },
            'trunc_params':{
                'svd_min': 1.e-12
            },
            'verbose': True
        }

        eng = dmrg.TwoSiteDMRGEngine(psi, M, dmrg_params)
        E, psi = eng.run()

        data = {
            'energy': E,
            'psi': psi,
            'model_params': model_params,
            'dmrg_params': dmrg_params
            }

        t2 = model_params['t2']
        with h5py.File("int_U_6_t2_" + f'{t2:.2f}' + "_V_" + f'{V:.2f}' +".h5", 'w') as f:
            hdf5_io.save_to_hdf5(f, data)
```

Bibliography

[1] P. W. Anderson. «More is different». In: *Science* **177** 4047 (Aug. 1972) (cit. on p. 2).

[2] D. R. Tilley and J. Tilley. *Superfluidity and Superconductivity.* New York, NY: Routledge, 1990 (cit. on p. 2).

[3] S. Balibar. «The enigma of supersolidity». In: *Nature* **464** (Mar. 2010), pp. 176–182 (cit. on pp. 2, 4, 8).

[4] J. F. Allen and A. D. Misener. «Flow of liquid helium II». In: *Nature* **141** 75 (Jan. 1938) (cit. on p. 2).

[5] P. Kapitza. «Viscosity of Liquid Helium below the λ-point». In: *Nature* **141** 74 (Jan. 1938) (cit. on p. 2).

[6] L. D. Landau. «Theory of the Superfluidity of Helium II». In: *Physical Review* **60** 356 (Aug. 1941) (cit. on p. 2).

[7] L. D. Landau. «On the Theory of Superfluidity». In: *Physical Review* **75** 884 (Mar. 1949) (cit. on p. 2).

[8] F. London. «The λ phenomenon of liquid helium and the Bose-Einstein degeneracy». In: *Nature* **141** (Jan. 1938), pp. 643–644 (cit. on p. 3).

[9] L. Tizsa. «Transport Phenomena in Helium II». In: *Nature* **141** 913 (Jan. 1938) (cit. on p. 3).

[10] O. Penrose. «On the quantum mechanics of helium II». In: *The London, Edinburgh, and Dublin Philosophical Magazine and Journal of Science* **42** (June 1951), pp. 1373–1377 (cit. on p. 3).

[11] J. Vannimenus and G. Toulouse. «Theory of the frustration effect. II. Ising spins on a square lattice». In: *Journal of Physics C: Solid State Physics* **10** L537 (Sept. 1977) (cit. on pp. 3, 31).

[12] E. Poli, T. Bland, S. J. M. White, M. J. Mark, F. Ferlaino, S. Trabucco, and M. Mannarelli. «Glitches in Rotating Supersolids». In: *Physical Review Letters* **131** 223401 (Nov. 2023) (cit. on p. 4).

[13] S. Balibar. «Supersolidity and superfluidity». In: *Contemporary Physics* **48** 1 (Jan. 2007), pp. 31–39 (cit. on p. 4).

[14] M. Boninsegni and N. V. Prokof'ev. «Supersolids: What and where are they?» In: *Reviews of Modern Physics* **84** 759 (May 2012) (cit. on p. 4).

[15] S. N. Bose. «Plancks Gesetz und Lichtquantenhypothese». In: *Zeitschrift für Physik* **26** (Dec. 1924), pp. 178–181 (cit. on p. 5).

[16] A. Einstein. «Quantentheorie des einatomigen idealen Gases». In: *Königliche Preußische Akademie der Wissenschaften. Sitzungsberichte* (July 1924), pp. 261–267 (cit. on p. 5).

[17] N. D. Mermin and H. Wagner. «Absence of Ferromagnetism or Antiferromagnetism in One- or Two-Dimensional Isotropic Heisenberg Models». In: *Physical Review Letters* **17** 1133 (Nov. 1966) (cit. on p. 6).

[18] S. Coleman. «There are no Goldstone bosons in two dimensions». In: *Communications in Mathematical Physics* **31** (Dec. 1973), pp. 259–264 (cit. on p. 6).

[19] O. Penrose and L. Onsager. «Bose-Einstein Condensation and Liquid Helium». In: *Physical Review* **104** 576 (Nov. 1956) (cit. on p. 6).

[20] E. P. Gross. «Unified Theory of Interacting Bosons». In: *Physical Review* **106** 161 (Apr. 1957) (cit. on p. 7).

[21] E. P. Gross. «Classical theory of boson wave fields». In: *Annals of Physics* **4** (May 1958), pp. 57–74 (cit. on p. 7).

[22] C. N. Yang. «Concept of Off-Diagonal Long-Range Order and the Quantum Phases of Liquid He and of Superconductors». In: *Reviews of Modern Physics* **34** 694 (Oct. 1962) (cit. on p. 7).

[23] A. J. Leggett. «Can a Solid Be Superfluid?» In: *Physical Review Letters* **25** 1543 (Nov. 1970) (cit. on p. 7).

[24] A. F. Andreev and I. M. Lifshitz. «Quantum Theory of Defects in Crystals». In: *Soviet Journal of Experimental and Theoretical Physics* **29** 1109 (Dec. 1969) (cit. on p. 7).

[25] G. V. Chester. «Speculations on Bose-Einstein Condensation and Quantum Crystals». In: *Physical Review A* **2** 1256 (July 1970) (cit. on p. 7).

[26] N. Prokof'ev and B. Svistunov. «Supersolid State of Matter». In: *Physical Review Letters* **94** 155302 (Apr. 2005) (cit. on p. 7).

[27] E. Kim and M. H. W. Chan. «Probable observation of a supersolid helium phase». In: *Nature* **427** (Jan. 2004), pp. 225–227 (cit. on p. 7).

[28] E. Kim and M. H. W. Chan. «Observation of Superflow in Solid Helium». In: *Science* **305** (Sept. 2004), pp. 1941–1944 (cit. on p. 7).

[29] N. Prokof'ev. «What makes a crystal supersolid?» In: *Advances in Physics* **57** (May 2007), pp. 381–402 (cit. on p. 8).

[30] A. S. C. Rittner and J. D. Reppy. «Observation of Classical Rotational Inertia and Nonclassical Supersolid Signals in Solid ^{4}He below 250 mK». In: *Physical Review Letters* **97** 165301 (Oct. 2006) (cit. on p. 8).

[31] A. S. C. Rittner and J. D. Reppy. «Disorder and the Supersolid State of Solid ^{4}He». In: *Physical Review Letters* **98** 175302 (Apr. 2007) (cit. on p. 8).

[32] S. Sasaki, R. Ishiguro, F. Caupin, H. J. Maris, and S. Balibar. «Superfluidity of grain boundaries and supersolid behavior». In: *Science* **313** (Aug. 2006), pp. 1098–1100 (cit. on p. 8).

[33] S. Sasaki, F. Caupin, and S. Balibar. «Wetting Properties of Grain Boundaries in Solid ^{4}He». In: *Physical Review Letters* **99** 205302 (Nov. 2007) (cit. on p. 8).

[34] J. Day and J. Beamish. «Low-temperature shear modulus changes in solid 4He and connection to supersolidity». In: *Nature* **450** 205302 (Dec. 2007), pp. 853–856 (cit. on p. 8).

[35] J. Day, O. Syshchenko, and J. Beamish. «Intrinsic and dislocation-induced elastic behavior of solid helium». In: *Physical Review B* **79** 214524 (June 2009) (cit. on p. 8).

[36] D. Y. Kim and M. H. W. Chan. «Absence of Supersolidity in Solid Helium in Porous Vycor Glass». In: *Physical Review Letters* **109** 155301 (Oct. 2012) (cit. on p. 8).

[37] D. Jaksch and P. Zoller. «The cold atom Hubbard toolbox». In: *Annals of Physics* **315** (Jan. 2005), pp. 52–79 (cit. on pp. 9, 24).

[38] C. Gross and I. Bloch. «Quantum simulations with ultracold atoms in optical lattices». In: *Science* **357** (Sept. 2017), pp. 995–1001 (cit. on p. 9).

[39] C. Chin, R. Grimm, P. Julienne, and E. Tiesinga. «Feshbach resonances in ultracold gases». In: *Reviews of Modern Physics* **82** 1225 (Apr. 2010) (cit. on pp. 9, 16).

[40] W. S. Bakr, J. I. Gillen, A. Peng, S. Fölling, and M. Greiner. «A quantum gas microscope for detecting single atoms in a Hubbard-regime optical lattice». In: *Nature* **462** (Nov. 2009), pp. 74–77 (cit. on p. 10).

[41] J. F. Sherson, C. Weitenberg, M. Endres, M. Cheneau, I. Bloch, and S. Kuhr. «Single-atom-resolved fluorescence imaging of an atomic Mott insulator». In: *Nature* **467** (Aug. 2010), pp. 68–72 (cit. on p. 10).

[42] M. Greiner, O. Mandel, T. Esslinger, T. W. Hänsch, and I. Bloch. «Quantum phase transition from a superfluid to a Mott insulator in a gas of ultracold atoms». In: *Nature* **415** (Jan. 2002), pp. 29–44 (cit. on p. 10).

[43] J. Léonard, A. Morales, P. Zupancic, T. Esslinger, and T. Donner. «Supersolid formation in a quantum gas breaking a continuous translational symmetry». In: *Nature* **543** (Mar. 2017), pp. 87–90 (cit. on pp. 11–14).

[44] J. R. Li, J. Lee, W. Huang, S. Burchesky, B. Shteynas, F. C. Top, A. O. Jamison, and W. Ketterle. «A stripe phase with supersolid properties in spin–orbit-coupled Bose–Einstein condensates». In: *Nature* **543** (Mar. 2017), pp. 91–94 (cit. on pp. 13, 15, 16).

[45] H. Miyake, G. A. Siviloglou, G. Puentes, D. E. Pritchard, W. Ketterle, and D. M. Weld. «Bragg Scattering as a Probe of Atomic Wave Functions and Quantum Phase Transitions in Optical Lattices». In: *Physical Review Letters* **107** 175302 (Oct. 2011) (cit. on p. 13).

[46] L. Tanzi, E. Lucioni, F. Famà, J. Catani, A. Fioretti, C. Gabbanini, R. N. Bisset, L. Santos, and G. Modugno. «Observation of a dipolar quantum gas with metastable supersolid properties». In: *Physical Review Letters* **122** 130405 (Apr. 2019) (cit. on pp. 15, 19).

[47] A. Recati and S. Stringari. «Supersolidity in ultracold dipolar gases». In: *Nature Reviews Physics* **5** (Oct. 2023), pp. 735–743 (cit. on pp. 15, 48).

[48] L. Santos, G. V. Shlyapnikov, and M. Lewenstein. «Roton-Maxon Spectrum and Stability of Trapped Dipolar Bose-Einstein Condensates». In: *Physical Review Letters* **90** 250403 (June 2003) (cit. on p. 16).

[49] R. N. Bisset, P. B. Blakie, and S. Stringari. «Static-response theory and the roton-maxon spectrum of a flattened dipolar Bose-Einstein condensate». In: *Physical Review A* **100** 013620 (July 2019) (cit. on p. 16).

[50] H. Kadau, M. Schmitt, M. Wenzel, C. Wink, T. Maier nad I. Ferrier-Barbut, and T. Pfau. «Observing the Rosensweig instability of a quantum ferrofluid». In: *Nature* **530** (Feb. 2016), pp. 194–197 (cit. on pp. 16, 17).

[51] T. D. Lee, K. Huang, and C. N. Yang. «Eigenvalues and Eigenfunctions of a Bose System of Hard Spheres and Its Low-Temperature Properties». In: *Physical Review* **106** 1135 (June 1957) (cit. on p. 16).

[52] D. S. Petrov. «Quantum Mechanical Stabilization of a Collapsing Bose-Bose Mixture». In: *Physical Review Letters* **115** 155302 (Oct. 2015) (cit. on p. 16).

[53] I. Ferrier-Barbut, H. Kadau, M. Schmitt, M. Wenzel, and T. Pfau. «Observation of Quantum Droplets in a Strongly Dipolar Bose Gas». In: *Physical Review Letters* **116** 215301 (May 2016) (cit. on p. 16).

[54] M. Schmitt, M. Wenzel, F. Böttcher, I. Ferrier-Barbut, and T. Pfau. «Self-bound droplets of a dilute magnetic quantum liquid». In: *Nature* **539** (Nov. 2016), pp. 259–262 (cit. on p. 16).

[55] C. R. Cabrera, L. Tanzi, J. Sanz, B. Naylor, P. Thomas, P. Cheiney, and L. Tarruell. «Quantum liquid droplets in a mixture of Bose-Einstein condensates». In: *Physical Review Letters* **359** 6373 (Dec. 2017), pp. 301–304 (cit. on p. 16).

[56] G. Semeghini et al. «Self-Bound Quantum Droplets of Atomic Mixtures in Free Space». In: *Physical Review Letters* **120** 235301 (June 2018) (cit. on p. 16).

[57] S. M. Roccuzzo and F. Ancilotto. «Supersolid behavior of a dipolar Bose-Einstein condensate confined in a tube». In: *Physical Review A* **99** 041601(R) (Apr. 2019) (cit. on p. 17).

[58] F. Böttcher, J. N. Schmidt, M. Wenzel, J. Hertkorn, M. Guo, T. Langen, and T. Pfau. «Observation of a dipolar quantum gas with metastable supersolid properties». In: *Physical Review X* **9** 011051 (Mar. 2019) (cit. on pp. 17, 18).

[59] L. Chomaz et al. «Long-Lived and Transient Supersolid Behaviors in Dipolar Quantum Gases». In: *Physical Review X* **9** 021012 (Apr. 2019) (cit. on p. 20).

[60] T. Bland, E. Poli, C. Politi, L. Klaus, M. A. Norcia, F. Ferlaino, L. Santos, and R. N. Bisset. «Two-Dimensional Supersolid Formation in Dipolar Condensates». In: *Physical Review Letters* **128** 195302 (2022) (cit. on p. 21).

[61] M. A. Norcia, C. Politi, L. Klaus, E. Poli, M. Sohmen, M. J. Mark, R. N. Bisset, L. Santos, and F. Ferlaino. «Two-dimensional supersolidity in a dipolar quantum gas». In: *Nature* **596** (Aug. 2021), pp. 357–361 (cit. on p. 21).

[62] H. A. Gersch and G. C. Knollman. «Quantum Cell Model for Bosons». In: *Physical Review* **129** 959 (Jan. 1963) (cit. on p. 23).

[63] M. P. A. Fisher, P. B. Weichman, G. Grinstein, and D. S. Fisher. «Boson localization and the superfluid-insulator transition». In: *Physical Review B* **40** 546 (July 1989) (cit. on p. 23).

[64] T. D. Kühner, S. R. White, and H. Monien. «The one-dimensional Bose-Hubbard Model with nearest-neighbor interaction». In: *Physical Review B* **61** 12474 (May 2000) (cit. on pp. 25, 27).

[65] J. K. Freericks and H. Monien. «Phase diagram of the Bose-Hubbard Model». In: *Europhysics Letters* **26** 545 (1994) (cit. on p. 25).

[66] T. D. Kühner and H. Monien. «Phases of the one-dimensional Bose-Hubbard model». In: *Physical Review B* **58** R14741(R) (Dec. 1998) (cit. on p. 25).

[67] V. L. Berezinskii. «Destruction of Long-range Order in One-dimensional and Two-dimensional Systems Possessing a Continuous Symmetry Group. II. Quantum Systems». In: *Journal of Experimental and Theoretical Physics* **61** (Sept. 1971), pp. 1144–1156 (cit. on pp. 27, 65).

[68] J. M. Kosterlitz and D. J. Thouless. «Ordering, metastability and phase transitions in two-dimensional systems». In: *Journal of Physics C: Solid State Physics* **6** 1181 (Apr. 1973) (cit. on pp. 27, 65).

[69] S. Ejima, H. Fehske, F. Gebhard, K. zu Münster, M. Knap, E. Arrigoni, and W. von der Linden. «Characterization of Mott-insulating and superfluid phases in the one-dimensional Bose–Hubbard model». In: *Physical Review A* **85** 053644 (May 2012) (cit. on pp. 27, 28).

[70] D. Rossini and R. Fazio. «Phase diagram of the extended Bose Hubbard model». In: *New Journal of Physics* **14** 065012 (June 2012) (cit. on pp. 27, 29).

[71] K. Kottmann, A. Haller, A. Acín, G. E. Astrakharchik, and M. Lewenstein. «Supersolid-Superfluid phase separation in the extended Bose-Hubbard model». In: *Physical Review B* **104** 174514 (Nov. 2021) (cit. on pp. 28, 46).

[72] F. Pollmann, E. Berg, A. M. Turner, and M. Oshikawa. «Symmetry protection of topological phases in one-dimensional quantum spin systems». In: *Physical Review B* **85** 075125 (Feb. 2012) (cit. on p. 29).

[73] R. Moessner and A. P. Ramirez. «Geometrical Frustration». In: *Physics Today* **59** (Feb. 2006), pp. 24–29 (cit. on p. 31).

[74] G. H. Wannier. «Antiferromagnetism. The Triangular Ising Net». In: *Physical Review* **79** 357 (July 1950) (cit. on p. 31).

[75] X.-L. Qi and S.-C. Zhang. «Topological insulators and superconductors». In: *Reviews of Modern Physics* **83** 1057 (Oct. 2011) (cit. on p. 31).

[76] P. Lecheminant. *One-Dimensional Quantum Spin Liquids.* June 2003. URL: `https://doi.org/10.48550/arXiv.cond-mat/0306520` (cit. on pp. 31, 46).

[77] P. W. Anderson. «Resonating valence bonds: A new kind of insulator?» In: *Materials Research Bulletin* **8** (Feb. 1973), pp. 153–160 (cit. on p. 31).

[78] F. D. M. Haldane. «Spontaneous dimerization in the S-1/2 Heisenberg antiferromagnetic chain with competing interactions». In: *Physical Review B* **25** 4925(R) (Apr. 1982) (cit. on p. 31).

[79] S. Furukawa, M. Sato, S. Onoda, and A. Furusaki. «Ground-state phase diagram of a spin-1/2 frustrated ferromagnetic XXZ chain: Haldane dimer phase and gapped/gapless chiral phases». In: *Physical Review B* **86** 094417 (Sept. 2012) (cit. on pp. 31, 46).

[80] N. Read. «Conformal invariance of chiral edge theories». In: *Physical Review B* **79** 245304 (June 2009) (cit. on p. 32).

[81] D. Griffiths. *Introduction to Elementary Particles, 2nd, Revised Edition*. Wiley, Oct. 2008 (cit. on p. 32).

[82] B. Povh, K. Rith, C. Scholz, F. Zetsche, and W. Rodejohann. *Particles and Nuclei: An Introduction to the Physical Concepts*. Springer, 2006 (cit. on p. 32).

[83] C. S. Wu, E. Ambler, R. W. Hayward, D. D. Hoppes, and R. P. Hudson. «Experimental Test of Parity Conservation in Beta Decay». In: *Physical Review* **83** 1413 (Feb. 1957) (cit. on p. 32).

[84] M. A. DeMarco. «Chiral Phases on the Lattice». PhD thesis. Cambridge, MA: Massachusetts Institute of Technology, May 2022. URL: `https://hdl.handle.net/1721.1/150719` (cit. on p. 32).

[85] T. Ramos, B. Vermersch, P. Hauke, H. Pichler, and Peter Zoller. «Non-Markovian dynamics in chiral quantum networks with spins and photons». In: *Physical Review A* **93** 062104 (June 2016) (cit. on p. 32).

[86] M. A. Cazalilla, R. Citro, T. Giamarchi, E. Orignac, and M. Rigol. «One dimensional Bosons: From Condensed Matter Systems to Ultracold Gases». In: *Reviews of Modern Physics* **83** 1405 (Dec. 2011) (cit. on p. 33).

[87] J. E. Hirsch, R. L. Sugar, D. J. Scalapino, and R. Blankenbecler. «Monte Carlo simulations of one-dimensional fermion systems». In: *Physical Review B* **26** 5033 (Nov. 1982) (cit. on p. 33).

[88] A. W. Sandvik. «Stochastic series expansion method with operator-loop update». In: *Physical Review B* **59** R14157(R) (June 1999) (cit. on p. 33).

[89] S. R. White. «Density matrix formulation for quantum renormalization groups». In: *Physical Review Letters* **69** 2863 (Nov. 1992) (cit. on p. 34).

[90] S. R. White. «Density-matrix algorithms for quantum renormalization groups». In: *Physical Review B* **48** 10345 (Oct. 1993) (cit. on p. 34).

[91] G. De Chiara, M. Rizzi, D. Rossini, and S. Montangero. «Density Matrix Renormalization Group for Dummies». In: *Journal of Computational and Theoretical Nanoscience* **5** 7 (July 2008), pp. 1277–1288 (cit. on pp. 34, 37).

[92] U. Schöllwock. «The density-matrix renormalization group in the age of matrix product states». In: *Annals of Physics* **326** 1 (Jan. 2011) (cit. on pp. 34, 44).

[93] R. Orús. «A practical introduction to tensor networks: Matrix product states and projected entangled pair states». In: *Annals of Physics* **349** (Oct. 2014), pp. 117–158 (cit. on pp. 34, 39, 44).

[94] K. G. Wilson. «The renormalization group: Critical phenomena and the Kondo problem». In: *Reviews of Modern Physics* **47** 773 (Oct. 1975) (cit. on p. 34).

[95] H. R. Krishna-murthy, J. W. Wilkins, and K. G. Wilson. «Renormalization-group approach to the Anderson model of dilute magnetic alloys. I. Static properties for the symmetric case». In: *Physical Review B* **21** 1003 (Feb. 1980) (cit. on p. 34).

[96] C. Lanczos. «An Iteration Method for the Solution of the Eigenvalue Problem of Linear Differential and Integral Operators». In: *Journal of Research of the National Bureau of Standards* **45** 2133 (Oct. 1950) (cit. on p. 35).

[97] I. U. Ojalvo and M. Newman. «Vibration modes of large structures by an automatic matrix-reduction method». In: *AIAA Journal* **8** 7 (July 1970) (cit. on p. 35).

[98] M. Suzuki. «Relationship between d-Dimensional Quantal Spin Systems and (d+1)-Dimensional Ising Systems: Equivalence, Critical Exponents and Systematic Approximants of the Partition Function and Spin Correlations». In: *Progress of Theoretical Physics* **56** (Nov. 1976), pp. 1454–1469 (cit. on p. 38).

[99] H. F. Trotter. «On the product of semi-groups of operators». In: *Proceedings of the American Mathematical Society* **10** (Apr. 1959), pp. 545–551 (cit. on p. 38).

[100] D. Gobert, C. Kollath, U. Schollwöck, and G. Schütz. «Real-time dynamics in spin-1/2 chains with adaptive time-dependent density matrix renormalization group». In: *Physical Review E* **71** 036102 (Mar. 2005) (cit. on p. 38).

[101] K. Okunishi, Y. Hieida, and Y. Akutsu. «Universal asymptotic eigenvalue distribution of density matrices and corner transfer matrices in the thermodynamic limit». In: *Physical Review E* **59** R6227(R) (June 1999) (cit. on p. 38).

[102] M. C. Chung and I. Peschel. «Density-matrix spectra for two-dimensional quantum systems». In: *Physical Review B* **62** 4191 (Aug. 2000) (cit. on p. 38).

[103] M. C. Chung and I. Peschel. «Density-matrix spectra of solvable fermionic systems». In: *Physical Review B* **64** 064412 (July 2001) (cit. on p. 38).

[104] J. Eisert, M. Cramer, and M. B. Plenio. «Colloquium: Area laws for the entanglement entropy». In: *Reviews of Modern Physics* **82** 277 (Feb. 2010) (cit. on p. 38).

[105] G. Vidal. «Efficient Classical Simulation of Slightly Entangled Quantum Computations». In: *Physical Review Letters* **91** 147902 (Oct. 2003) (cit. on pp. 39, 43).

[106] G. Vidal. «Efficient Simulation of One-Dimensional Quantum Many-Body Systems». In: *Physical Review Letters* **93** 040502 (July 2004) (cit. on pp. 39, 43).

[107] G. Vidal. «Classical Simulation of Infinite-Size Quantum Lattice Systems in One Spatial Dimension». In: *Physical Review Letters* **98** 070201 (Feb. 2007) (cit. on pp. 39, 43).

[108] J. I. Cirac and F. Verstraete. «Renormalization and tensor product states in spin chains and lattices». In: *Journal of Physics A: Mathematical and Theoretical* **42** 504004 (Dec. 2009) (cit. on p. 39).

[109] F. Verstraete, V. Murg, and J. I. Cirac. «Matrix product states, projected entangled pair states, and variational renormalization group methods for quantum spin systems». In: *Advances in Physics* **57** (July 2008), pp. 143–224 (cit. on p. 39).

[110] S. S. Roy, L. Carl, and P. Hauke. «Genuine multipartite entanglement in a one-dimensional Bose-Hubbard model with frustrated hopping». In: *Physical Review B* **106** 195158 (Nov. 2022) (cit. on p. 46).

[111] N. Baldelli, C. R. Cabrera, S. Julia-Farré, M. Aidelsburger, and L. Barbiero. *Frustrated extended Bose-Hubbard model and deconfined quantum critical points with optical lattices at the anti-magic wavelength.* Sept. 2023. URL: `https://doi.org/10.48550/arXiv.2309.03193` (cit. on pp. 46–48).

[112] S. Greschner, L. Santos, and T. Vekua. «Ultra-cold bosons in zig-zag optical lattices». In: *Physical Review A* **87** 033609 (Mar. 2013) (cit. on pp. 46, 56).

[113] T. Mishra, R. V. Pai, S. Ramanan, M. S. Luthra, and B. P. Das. «Supersolid and solitonic phases in the one-dimensional extended Bose-Hubbard model». In: *Physical Review B* **80** 043614 (Oct. 2009) (cit. on p. 46).

[114] J. Hauschild and F. Pollmann. «Efficient numerical simulations with Tensor Networks: Tensor Network Python (TeNPy)». In: *SciPost Physics Lecture Notes* **5** (Oct. 2018) (cit. on p. 50).